Materials Science & Engineering R 167 (2026) 101087

Contents lists available at ScienceDirect

Materials Science & Engineering R

journal homepage: www.elsevier.com/locate/mser

Emerging MXene and covalent-organic framework hybrids: Design strategies for energy, sensing, and environmental applications

Farzad Seidi [a,*,1], Ahmad Arabi Shamsabadi [b,1], Mostafa Dadashi Firouzjaei [c], Mark Elliott [c], Anupma Thakur [d], Yang Huang [a], Yuqian Liu [a], Huining Xiao [e,*], Babak Anasori [d,f,**]

[a] Jiangsu Co-Innovation Center of Efficient Processing and Utilization of Forest Resources and International Innovation Center for Forest Chemicals and Materials, Nanjing Forestry University, Nanjing 210037, China
[b] Department of Chemistry, University of Pennsylvania, Philadelphia, PA 19104, USA
[c] Department of Civil, Construction, and Environmental Engineering, University of Alabama, Tuscaloosa, AL 35487, USA
[d] School of Materials Engineering, Purdue University, West Lafayette, IN 47907, USA
[e] Department of Chemical Engineering, University of New Brunswick, Fredericton, New Brunswick E3B 5A3, Canada
[f] School of Mechanical Engineering, Purdue University, West Lafayette, IN 47907, USA

ARTICLE INFO

Keywords:
MXene
Covalent organic framework
Hybrid
Conductivity
And porosity

ABSTRACT

The demand for developing advanced hybrid materials with improved functions and performance is rising due to the current challenges in the environmental and energy fields. Hybridization of nanomaterials can address the shortcomings of individual components and afford composite nanomaterials with improved performance through synergistic effects. MXenes are among the growing families of inorganic two-dimensional (2D) materials with unique properties such as high electrical conductivity, hydrophilicity, easy processability, and excellent photothermal and electrochemical characteristics. Some limitations of MXenes, including poor chemical stability in oxidative conditions and low porosity due to restacking the 2D flakes, could hinder their potential in environmental applications. On the other hand, covalent organic frameworks (COFs) are highly porous organic networks but with primary shortcomings of low electrical conductivity and poor processability. Combining the metallic conductivity and excellent photothermal and electrochemical properties of MXenes with the high porosity of COFs enables the formation of COF@MXene nanomaterials with improved properties. Here, we provide a comprehensive review of the strategies utilized for designing and fabricating COF@MXene heterostructures through chemical and physical hybridization. The synergistic effects of hybridization are discussed for diverse applications, including catalysis, energy storage materials, sensors, water purification, and anti-corrosion coatings. Finally, the future outlook of the COF@MXenes, their challenges and possible solutions for these challenges are discussed.

1. Introduction

The growth of science and technology in today's life has led to a swift rise in the demand for materials with outstanding features. Hybrid materials combine the properties of individual components to provide remarkable properties from the synergistic effect. Hybrid materials have been developed on different scales, including macro, micro, and nanoscales [1,2]. Combining different components creates unique structures with improved properties and performance. The engineering materials at different scales can afford synergistic effects and endow the unique characteristics for specific applications. The impact of synergistic effects at the nanoscale is much stronger than that at the macro and microscales due to the larger surface area at the nanoscale [3]. In nanoscience, different types of hybrid nanomaterials have been developed by chemical or physical engineering [4–6]. Surface and interfacial engineering of nanomaterials with organic compounds provides new opportunities for broader applications of nanomaterials. For instance, surface-initiated polymerization on nanomaterials is a straightforward and effective strategy for generating organic-inorganic hybrid nanomaterials [7,8]. Most pristine inorganic nanomaterials have weak stabilities in nonpolar

---

* Corresponding authors.
** Corresponding author at: School of Materials Engineering, Purdue University, West Lafayette, IN 47907, USA.
E-mail addresses: f_seidi@njfu.edu.cn (F. Seidi), hxiao@unb.ca (H. Xiao), banasori@purdue.edu (B. Anasori).
[1] These authors contributed equally to this work.

https://doi.org/10.1016/j.mser.2025.101087
Received 23 February 2025; Received in revised form 5 July 2025; Accepted 14 August 2025

and non-aqueous environments. However, grafting of hydrophobic polymers onto the surface of nanomaterials effectively alters the stability tendency of these nanomaterials, shifting from polar to nonpolar media. An alternative strategy is the fabrication of hybrid nanomaterials through the combination of two or more individual nanomaterials, such as covalent organic framework (COF)/graphene [9], COF/metal-organic framework (MOF) [10], MOF/graphene [11], and MOF/MXene [12] hybrids. These hybrid nanostructures have found wide applications in catalysis [13], sensing [14], medical [15,16], environmental and energy technologies [17–19].

This review describes the strategies for preparing hybrid materials from MXenes and COFs through chemical and physical processes. The improved properties of these hybrid nanostructures compared to individual MXene or COF nanomaterials are discussed in different applications, including medical, energy storage, water treatment, and sensors. Finally, the outlook and future directions of COF@MXene hybrids and the related challenges are highlighted and discussed. So far, only one review article has been published on COFs/MXenes composites [20]. However, in such a rapidly evolving research area, we found a need for a comprehensive coverage of all the studies in the field (and the new ones since 2023) with an in-depth critical analysis. Our manuscript provides a comprehensive and critical overview of the preparation methods for COF@MXene hybrids, offering comparative insights into their advantages and limitations. Beyond synthesis strategies, their broad applications have been broadly discussed.

2. MXenes: Structure, Synthesis, and Unique Properties

The MXenes family is one of the largest groups of two-dimensional (2D) nanomaterials developed in the past decade [21,22]. MXenes are transition metal carbides, nitrides, and carbonitrides with the general $M_{n+1}X_nT_x$ formula in which M represents an early transition metal (such as Ti, V, Nb, and Mo), X stands for carbon and/or nitrogen, n is 1–4, and T_x refers to the MXenes' terminal groups (-F, -Cl, -OH, -O, etc.) [22–24].

2.1. *Approaches for MXene Synthesis: Selective Etching and Beyond*

Commonly, most MXenes are synthesized from the chemical selective etching of MAX phases with $M_{n+1}AX_n$ general formula, in which A denotes an element from IIIA and IVA groups in the periodic table (such as Al and Si). While there are numerous types of MXenes [25,26], titanium carbide ($Ti_3C_2T_x$) is the most studied one. The first MXene was multilayer $Ti_3C_2T_x$ synthesized by the selective removal of the Al layer of Ti_3AlC_2 through chemical etching using a hydrofluoric acid (HF) solution [23] (Fig. 1). The subsequent delamination by chemical intercalation or mechanical exfoliation creates the monolayer MXene nanosheets. Different etching procedures have been developed that result in differences in flake size, defects, and surface functional groups [27]. Most of the MXene/COF hybrids are typically synthesized using $Ti_3C_2T_x$. A recent study reported utilization a pioneering chemical-scissor-mediated intercalation chemistry technique for manipulating the structure of three-dimensional (3D) non-van der Waals (non-vdW) MAX phases and 2D vdW MXenes [28]. By employing a combination of Lewis acidic molten salt (LAMS) and metal scissors for structural modification, the MAX phases and MXenes are exfoliated directly into stacked lamellae within molten salts [28–30]. This pioneering technique has revealed a remarkable collection of 2D metal-intercalated layered carbides. The chemical transformation and bottom-up preparation are the other common approaches for the MXenes fabrication [31,32]. Deoxygenation and carburization [33], ammoniation of transition metal carbides [34], and carburization of transition metal sulfides [31] are other chemical transformation approaches for MXenes synthesis. Bottom-up methods include chemical vapor deposition (CVD) and salt-templated growth. MXenes can also be synthesized by direct reaction of metals and metal halides with graphite,

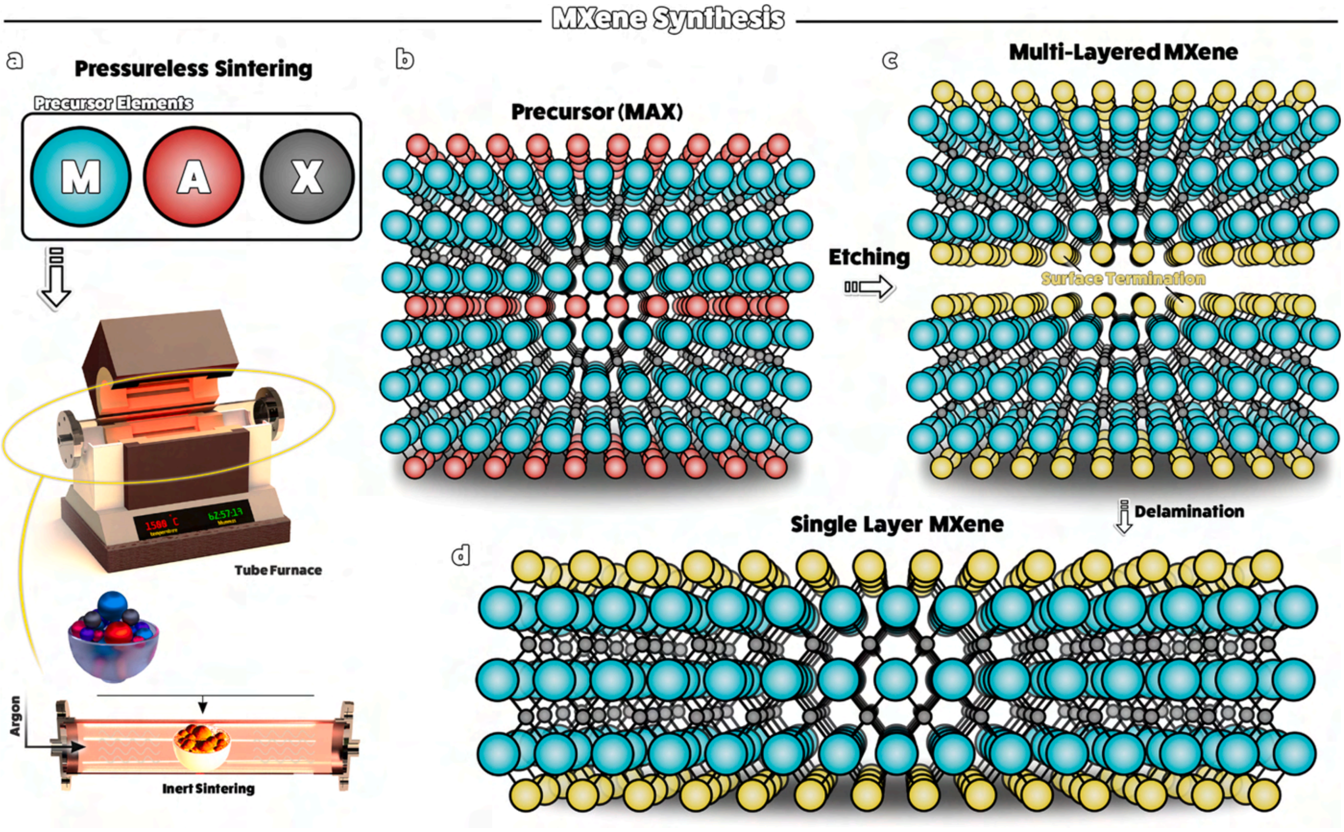

Fig. 1. The schematic illustration for synthesizing MXenes using selective etching [48]. Reproduced with permission from Elsevier.

methane, or nitrogen [30]. This process allows for the CVD growth of MXene layers and the formation of complex spherulite-like morphologies. However, the production of large-area, high-quality ultra-thin films by CVD remains a significant challenge. Additionally, visible defects are generated on the materials produced by the salt template method [35]. The synthesis and processing of MXenes have already been discussed in several reviews and papers [36–40].

MXenes with adjustable properties can be prepared by varying the elemental composition, atomic structure, and synthesis methods. The properties of MXenes, including metal-like conductivity [41], electronic, optical, and antimicrobial activity[42], make them excellent nanomaterials for developing advanced materials.

Due to their adjustable architectures, strong light absorption, and outstanding bulk electrical conductivity (~ 20000–24000 S/cm for $Ti_3C_2T_x$), MXenes have the potential for catalysis and energy storage applications [39,43,44]. MXenes have provided new opportunities in the separation technologies due to their hydrophilicity (water contact angles of 20–30° for $Ti_3C_2T_x$ and Ti_2CT_x films), diverse core and surface chemistry (-F, -Cl, -OH, and -O functional groups), antibacterial features, and mechanical strength (mechanical stiffness at 300–400 GPa) [45,46]. The emergence of MXenes as an advanced sensing and biosensing platform is mainly attributed to their high metal-like electrical conductivity, biocompatibility, ion-transport capability, and straightforward functionalization [47]. Their excellent dispersibility in various solvents (thanks to a negative surface charge), strong interfacial bonds, customizable surface chemistry, and compatibility with polymers make MXenes highly suitable for creating anti-corrosion coatings.

2.2. *Enhancing MXenes: Surface Functionalization Methods*

Generally, the surface of MXenes is covered with polar functional groups (such as -OH, -O, -Cl, and -F), which render MXenes highly hydrophilic and excellent colloidal stability in aqueous media [49,50]. However, exposure of MXenes to an oxidative environment leads to structural changes and transformation into metal oxides and releases gases, including CH_4, CO, CO_2, and HF [51]. Surface functionalization can change the properties of the MXenes and increase their chemical stability due to the reduced hydrophilicity and steric stabilization of long chains of modifiers [52]. Surface functionalization of MXenes can be achieved through covalent or non-covalent modifications. Several reviews discuss surface functionalization strategies for MXenes [53,54]. The functionalization proceeds via interactions either with polar surface groups or directly with M (the transition metal) of the nanosheets. The most common utilized methods for the functionalization of MXenes' surface are depicted in Fig. 2.

Covalent Conjugation: In this strategy, the modifier agent is attached to the MXene via the formation of covalent bonds. The silanization (Fig. 2b) is a facile strategy for incorporating various functional groups into the surface of MXenes. Hydrolysis of silanes forms the Si-OH bonds and subsequently by condensation with the M-OH groups on the MXene surfaces forms the covalent M-O-Si bonds. For instance, the functionalization of the $Ti_3C_2T_x$ surface with an aminosilane agent forms the NH_2-$Ti_3C_2T_x$ nanosheets and changes the surface charge from negative to positive at neutral pH [55–57]. A one-step method of $Ti_3C_2T_x$ carboxylation by reaction with chloroacetic acid could incorporate COOH groups on the MXene surface [58] and lead to a negative surface charge of −54 mV at pH 8. Indeed, the carboxylation increases the negative surface charge of $Ti_3C_2T_x$ and improves the chemical oxidative resistance of the nanosheets.

Phenyl diazonium salts (Ph-N≡N$^+$) are another group of surface-modifying agents. Some of the -OH groups of MXenes are converted into Ph-O-M groups by reaction with the diazo agents (Fig. 2c). Phenyl

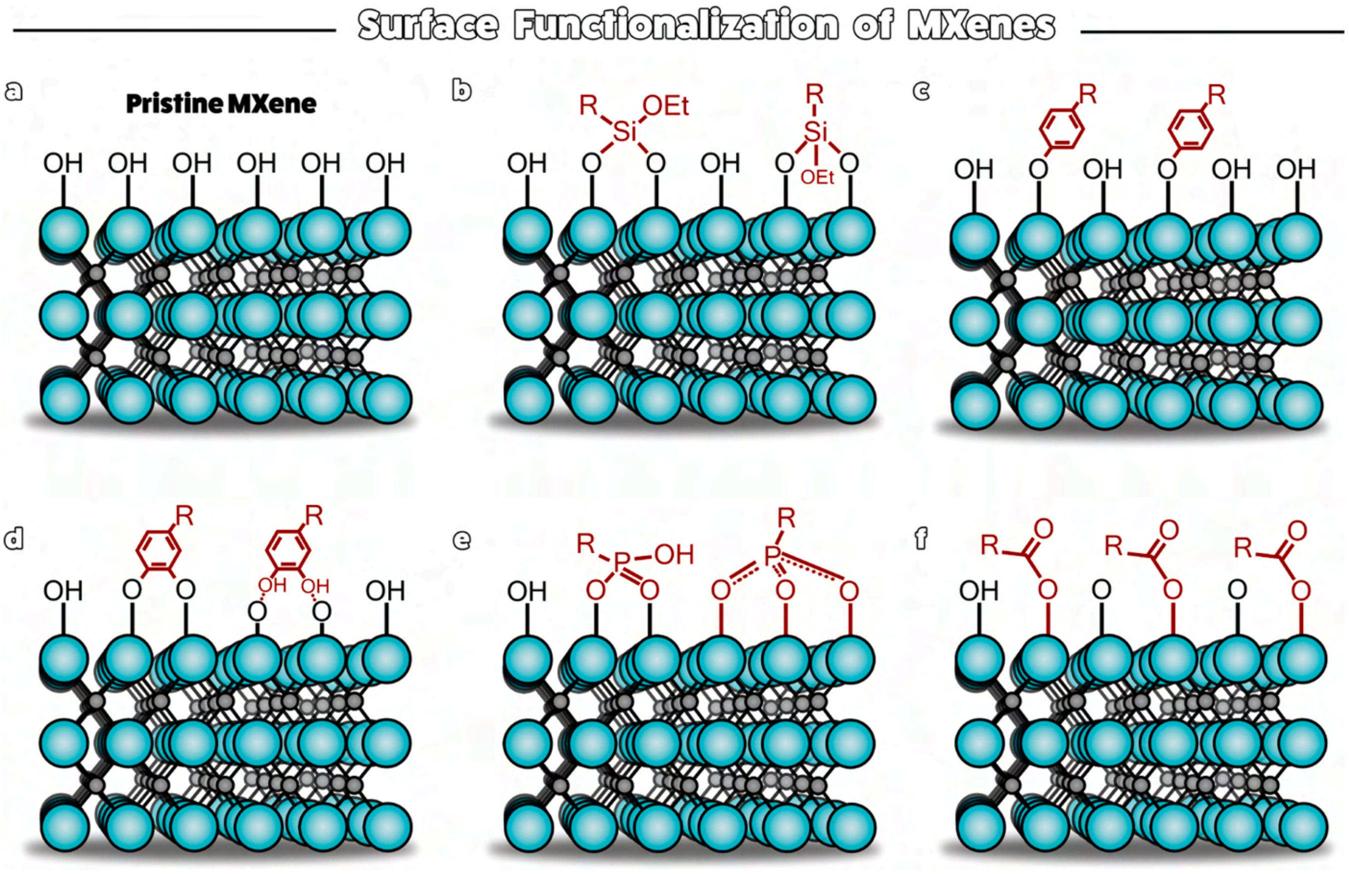

Fig. 2. Simplified description for the surface functionalization of MXene nanosheets through reactions with (b) alkyl silanes, (c) aryl diazonium salts, (d) catechols, (e) alkyl phosphates, and (f) alkyl carboxylates.

diazonium salts are unstable compounds that can be produced *in situ* in aqueous media by treating the phenyl amines (Ph-NH_2) with $NaNO_2$/HCl [59]. MXenes functionalized with phenyl sulfonic acid (-PhSO_3H) [60,61] and phenyl carboxylic acid (-PhCOOH) [62] groups were obtained, respectively, by reactions of MXene nanosheets with sulfanilic acid/$NaNO_2$ and 4-aminobenzoic acid/$NaNO_2$ via the *in situ* formation of the diazonium salt.

Ligand-Metal Functionalization: Due to the presence of the transition metal(s) in the MXenes structures, a variety of ligands can anchor on the MXene surface through the formation of ligand-metal complexes. Catechols, phosphates, and carboxylates can create strong metal-ligand interactions. Besides the H-bonding between catechol and the MXenes surface, catechol-based compounds can attach to the surface of MXenes via the metal-ligand interaction between the transition metal of the MXene with the -OH groups of a catechol moiety (for example, alkylated 3,4-dihydroxy-l-phenylalanine (ADOPA) or polydopamine) (Fig. 2d) [63,64].

Phosphate-based organic ligands are another type of surface modifiers used to manipulate the surface of MXene nanosheets by forming P-O-M (M: metal) bonds [65]. Organic phosphonic acids (R-PO$(OH)_2$) can generate two or three bonds with the metal surface (Fig. 2e). Anchoring alkyl phosphonic acids on the MXene surface can change the hydrophilicity and dispersibility of nanosheets in solvents [66,67].

Alkyl carboxylates are another group of ligands used for engineering the MXene surface (Fig. 2f) [68]. However, carboxylates are weaker ligands compared to catechols and phosphates. Up to 14 wt% carboxyl-terminated polyethylene glycol (PEG-COOH) could be grafted to the surface of $Ti_3C_2T_x$ MXene flakes, which improved the oxidation resistance, hydrophobicity (increased contact angle from 65 to 93°), and dispersibility in organic solvents [69].

Electrostatic Interaction: MXene surfaces are negatively charged, whereas their edges are positively charged [70]. Therefore, based on electrostatic interactions, edges can be modified selectively using anionic compounds, while the surfaces can be functionalized selectively with cationic modifiers. Cationic surfactants like cetyltrimethylammonium bromide (CTAB) can be anchored to the surface of MXenes to improve their dispersibility in organic solvents [71,72].

Although various strategies have been used for the modification of the MXene surface, only a few of them are practically applicable for industrial applications, considering factors such as scalability, reproducibility, and cost-effectiveness. Catechol-based ligands are introduced as universal ligands for scale-up surface modification of MXene dispersions [73]. Due to the strong H-bonding and π-electron interactions between the catechol head and surface terminal groups of MXenes, these ligands can functionalize MXene surfaces under mild reaction conditions (room temperature and moderate pH) without affecting the MXene properties. By using catechols bearing superhydrophobic tails (such as fluorinated alkyl tails), the surface of MXenes can shift from hydrophilic to superhydrophobic. The surfaces of different MXenes, including Ti_2CT_x, Nb_2CT_x, V_2CT_x, Mo_2CT_x, $Ti_3C_2T_x$, Ti_3CNT_x, $Mo_2TiC_2T_x$, $Mo_2Ti_2C_3T_x$, and $Ti_4N_3T_x$, are successfully functionalized by treating with catechol ligands at a scalable level for mass production with almost 100 % yield [73]. In addition to the catechol-based ligands, positively charged macromolecules have been proven to be suitable agents for large-scale modification of the MXene surface. For instance, poly(diallyldimethylammonium chloride) has been successfully utilized for the large-scale fabrication of positively charged MXene membranes [74].

Strong adhesion between MXene and COFs can be achieved by pre-functionalizing the MXene surface with a functional group utilized in the COF formation. Among the surface modification techniques described in Fig. 2, the covalent conjugation has been used to modify the MXene surface. The MXene silanization with an amino silane agent renders the formation of MXene-NH_2, which is the only method utilized for pre-functionalizing MXene to enable its subsequent covalent attachment with COFs. However, the other different methods described in Fig. 2 have the potential for pre-functionalizing MXene and utilization in future studies to design alternative MXene/COF hybrids.

3. COFs: Crystalline Frameworks with Tunable Porosity

COFs are metal-free analogues of metal-organic frameworks (MOFs) with highly porous crystalline structures that are prepared via covalent bond conjugation of organic molecules [75]. The COFs' pore size can be tuned by controlling building block size, type, and chemistry. Using different building blocks in the COFs provides a diverse range of functionalities. The low density and diverse functionality of COFs distinguish them from other porous crystalline compounds.

The fabrication of ordered and crystalline COFs requires the utilization of precursors that can form reversible bonds while preserving their geometry in the COF structure. Reversible bonds such as imines, hydrazones, and boronate esters are the main linkages used to synthesize COFs. Precursors with amino (-NH_2) and aldehyde (-CHO) groups are among the main building blocks employed for COFs fabrication (Figures S1 and S2). Similar structures with boronic acid, -B$(OH)_2$, groups have been used to prepare COFs by conjugating with various catechol-based building blocks. The presence of multiple functional groups in COFs enables them for different post-functionalization processes. This flexibility makes the COF suitable for the formation of hybrids with other nanomaterials. Based on the geometry of the building blocks, both 2D and 3D COF structures have been synthesized. The building blocks are generally named C_2, C_3, and so on, based on the number of bonds each precursor can generate (Fig. 3). In 2D COFs, the planar geometry of the building blocks leads to the formation of layered structures like MXenes and graphene (Fig. 3). In 3D COFs, at least one of the building blocks has an orthogonal (T_d) structure (Figure S3). The fabrication of MXene/COF hybrid materials using 3D COF has not been reported yet. The reason is probably related to the weaker interactions between 2D MXene nanosheets with 3D COFs compared to the stronger interactions with 2D COFs materials.

The production of COFs through the reversible reactions leads to the formation of thermodynamically stable networks and provides the COFs with self-healing properties. However, there are several reports on the synthesis of COFs from irreversible reactions [76–78]. The main COFs synthesis methods are solvothermal [79], microwave [80], ionothermal [81], and mechanochemical [82] synthesis . Importantly, COFs with adjustable thickness can be obtained by the interfacial synthesis methods [83]. COFs have found vast applications in different areas, including in semiconductors [84], sensors[85], energy storage [86–89], adsorption and separation processes [90,91], and catalysis [92,93]. The fabrication of hybrid materials with synergistic properties and improved performance is always of great interest. Therefore, diverse types of COFs-based hybrid materials have been prepared by hybridization of COFs with various substrates such as Al_2O_3 [94], Fe_3O_4 [95], graphene [96], and silicon [97].

4. Engineering COF@MXene Hybrids: Design and Integration Methods

Combination of the metal-like electrical conductivity, photothermal, and electrothermal properties of MXenes with tunable porosity of COFs form novel hybrid materials with excellent properties for various applications including catalysis, energy storage, separation, sensing, and anti-corrosion coatings. Typically, there are three methods for fabricating COF@MXene hybrid materials (Fig. 4).

4.1. Physical Hybridization of COFs and MXenes

The simplest method for the fabrication of COF@MXene hybrids is mixing dispersions of a pre-fabricated COF with MXene nanosheets (Fig. 4a). The interaction between COFs and MXenes is mainly electrostatic, as discussed earlier. MXenes are negatively charged, whereas COFs with high contents of nitrogen groups usually are positively

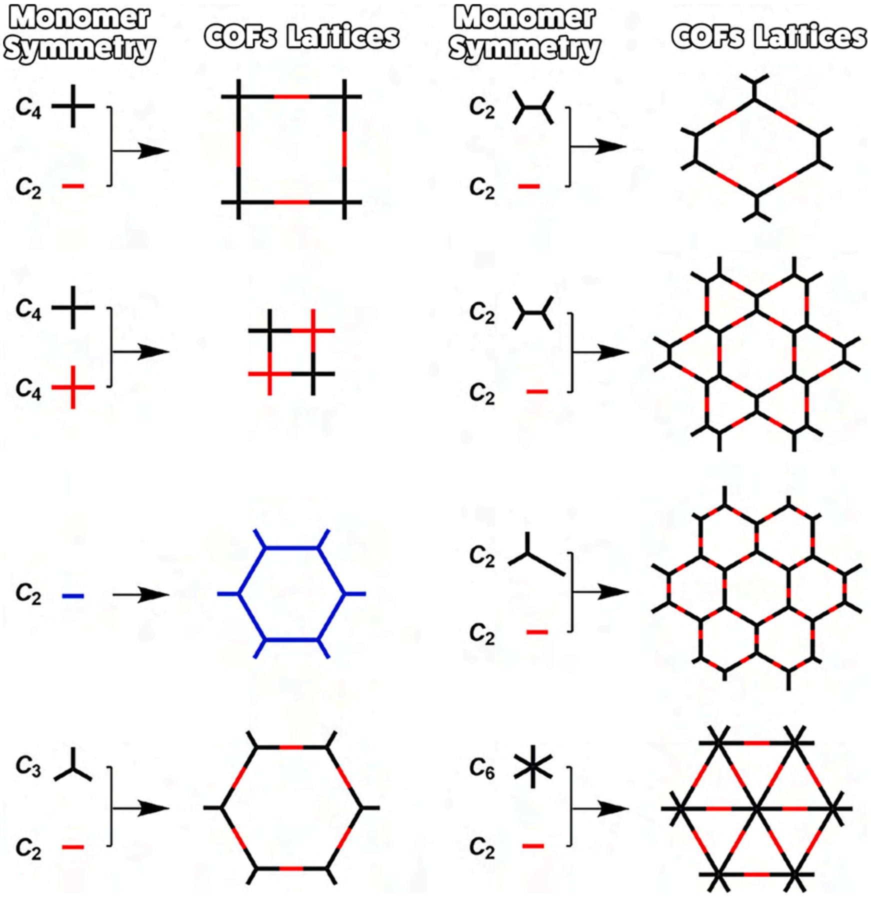

Fig. 3. The schematic topological diagrams for the fabrication of 2D COFs [98]. Reproduced with Permission from American Chemical Society, 2020.

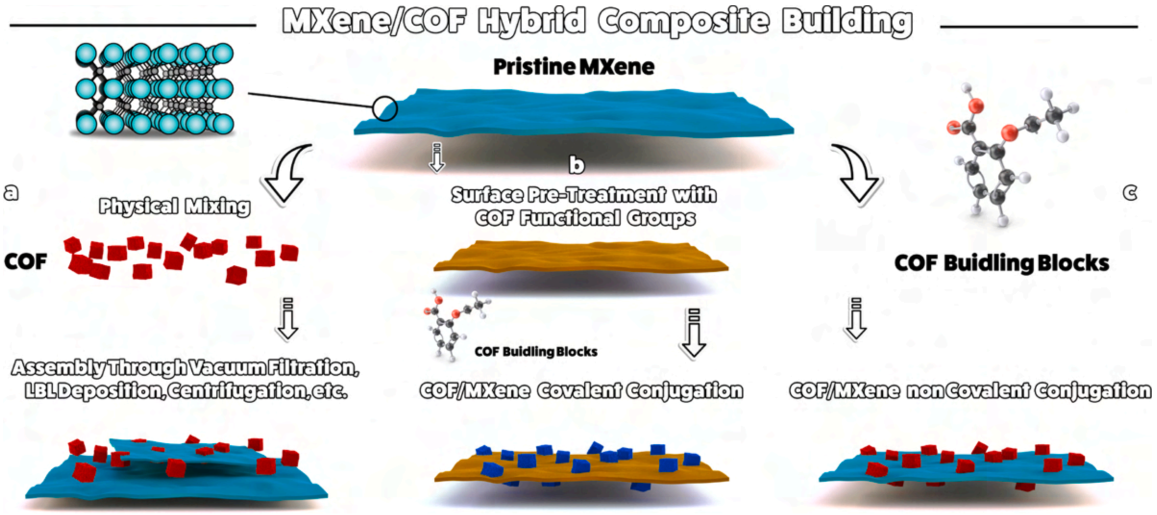

Fig. 4. Strategies for the fabrication of COF@MXene hybrid composites include (a) physical mixing of a pre-fabricated COF and MXene, (b) *in-situ* growth of COF on the surface of a functionalized MXene through covalent conjugation, and (c) *in-situ* growth of COF on the surface of a pristine MXene through non-covalent conjugation.

charged. However, this strategy provides the weakest interaction between COFs and MXenes, so that the performance of resulting COF@MXene composites is not high. Table S1 summarizes the fabrication of COF@MXene through their physical mixing and the application of each composite. Vacuum filtration of physically mixed dispersions of COFs with MXenes is the most used and straightforward method in this category for making films. Alternatively, sequential vacuum filtration of COF dispersions and MXenes dispersions can provide multilayer films.

4.2. *In-Situ Growth and Covalent Linking of COFs on MXenes*

In this approach, a COF is synthesized by condensation of its precursors in the presence of a MXene (Fig. 4b). To covalently conjugate COFs with MXenes, the surfaces of MXene nanosheets are pre-functionalized with one of the precursor functional groups used in COFs synthesis (Table S2).[99,100] For instance, if a COF is prepared by condensing building blocks with amino (-NH_2) and aldehyde (-CHO) groups, the surface of MXene is pre-functionalized with either -NH_2 or -CHO groups. As described in Section 2.1, the surface of MXene can be aminated using various reagents. The most utilized reagents are amino silanes that can form NH_2-$Ti_3C_2T_x$ nanosheets [101]. Additionally, even simple mixing of $Ti_3C_2T_x$ nanosheets with amino-based building blocks of COFs can lead to stable hybrids due to the strong H-bonding interactions between these building blocks with the MXene surface. Table S2 lists some of these methods. Utilizing an ionothermal method for the in-situ growth of COF on the surface of MXene can produce covalent Ti-N linkages between the COF and MXene, even without pre-modifying the MXene [102]. For instance, a COF@$Ti_3C_2T_x$ heteroconjugate was prepared through ionothermal catalytic polymerization of 1,4-dicyanobenzene (DCB) in the presence of $Ti_3C_2T_x$ in molten $ZnCl_2$ as both catalyst and solvent at 400 °C [102]. The formation of Ti-N bonds at the interface between COF and $Ti_3C_2T_x$ MXene was proved from operando X-ray absorption near edge spectroscopy (XANES) and X-ray photoelectron spectroscopy (XPS) data. The high temperature of the ionothermal process probably facilitates the formation of Ti-N linkages.

The 2D structure of MXenes assists the COF growth on its surface to form vertically aligned π-columns [103,104]. However, due to the lower surface area of MXenes than COFs, increasing the MXene content reduced the BET surface area of the hybrid material. The nitrogen adsorption-desorption isotherms confirmed a specific surface area of 20 and 565 $m^2\ g^{-1}$ for the pristine $Ti_3C_2T_x$ MXene and COF@$Ti_3C_2T_x$ heteroconjugate [105]. The *in-situ* growth of COFs on the surface of MXenes can be detected by SEM analysis. For instance, heteroconjugation of $Ti_3C_2T_x$ MXene with COFs (made of 2,5-diethoxyterephthalohydrazide and 1,3,5-triformylbenzene) showed the formation of nanoflower-shaped hydrazone-linked COFs on the MXenes surface (SEM image Fig. 5a-c)[105].

Although MXene and aminosilane functionalized MXene nanosheets usually show a smooth surface, however, the surface of a COF@MXene (prepared by in situ growth of 1,3,5-triformylbenzene (TFB) and p-phenylenediamine (PDA) on the surface of NH_2-$Ti_3C_2T_x$) is rough, indicating the porous structure of the COF layer (Fig. 6a-c). The uniform growth of the COF on the MXenes surface can be proved by recording the elemental mapping images (Fig. 6d). Additionally, the BET surface area of $Ti_3C_2T_x$ MXenes was 25 $m^2\ g^{-1}$, which increased to 239 $m^2\ g^{-1}$ for the COF@$Ti_3C_2T_x$ heteroconjugate. Micropores (1.6–1.8 nm) resulted from the COFs, and mesopores (2–40 nm) originated from the 3D structure through COFs intercalation between the MXene layers (Fig. 6e).

4.3. *Non-Covalent Strategies for In Situ COF@MXene Hybrids*

Adding pristine MXenes to the precursors used to synthesize COFs can lead to the *in-situ* fabrication of COF, which are usually attached to the surface of the MXene through electrostatic interactions (Fig. 4c, Table S3). The positively charged COFs can generate strong electrostatic interactions with MXene, which leads to improved interface adhesion. For instance, the *in situ* condensation of triaminoguanidine hydrochloride with 1,3,5-triformylphloroglucinol in the presence of $Ti_3C_2T_x$ MXene nanosheets led to the formation and ionically adsorption of cationic guanidinium-based COFs on the surface of MXenes (Fig. 7a) [107]. While pristine MXenes showed a smooth surface, the COFs@MXene hybrid showed a rough and tremella-like morphology (Fig. 7b-c). The elemental mappings confirmed the uniform growth of the COFs on the MXene surface (Fig. 7d). Practically, this method is less effective than the covalent conjugation of MXenes to COFs (method two) but more effective than the physically mixed pre-fabricated COFs with MXenes (method one). Indeed, covalently linked MXenes with COFs provide the highest synergistic effect, whereas the physical mixing of pre-fabricated COFs with MXenes affords the weakest interactions between the two components [99].

While different methods for the synthesis of COF@MXene hybrids have been developed, the mass production and scaling-up fabrication of COF@MXene is still challenging. One of the key factors in all synthesis strategies is to guarantee that COF can completely and uniformly cover the whole surface of MXene nanosheets. The uncovered areas can suffer from oxidation with exposure to oxygen and therefore the performance of the COF@MXene hybrid can decline gradually. Furthermore, each strategy for the fabrication of COF@MXene hybrids could have its own drawbacks. For instance, in the first strategy that utilizes physical hybridization of COFs and MXenes, the interactions between COF and MXene are weak, which results in the vulnerability of the COF@MXene hybrid toward environmental influences. For example, the oxygen diffusion onto the MXene surface can weaken the COF@MXene performance due to the gradual oxidation of the MXene segment. In the second and third strategies, COF is synthesized in situ in the presence of MXene nanosheets. A long reaction time, high temperature, and inert atmosphere are necessary for the fabrication of COF@MXene hybrids. These harsh conditions increase the construction cost and also put MXenes at risk of structural degradation.

5. COF@MXene Hybrids: Applications across Industries

5.1. *Catalytic Innovations Using COF@MXene Hybrids*

The synergistic effects between COFs and MXenes results in COF@MXene hybrid materials with strong performance in different catalysis processes. This section discusses the catalysis applications of COF@MXene hybrids, including photocatalytic H_2 evolution [99,108], photocatalytic H_2O_2 production [109], photocatalytic NAHD regeneration for CO_2 reduction process [110–112], photocatalytic antibacterial [113,114], electrocatalytic H_2 evolution [105,115], electrocatalytic nitrogen reduction reaction (NRR) [116], and electrocatalytic methanol oxidation [117]. An assessment of the effectiveness of COF@MXene hybrids as catalysts in diverse applications is provided in Table S4.

5.1.1. *COF@MXene Hybrids as Photocatalysts*

While COFs are suitable platforms with tunable functionalities in

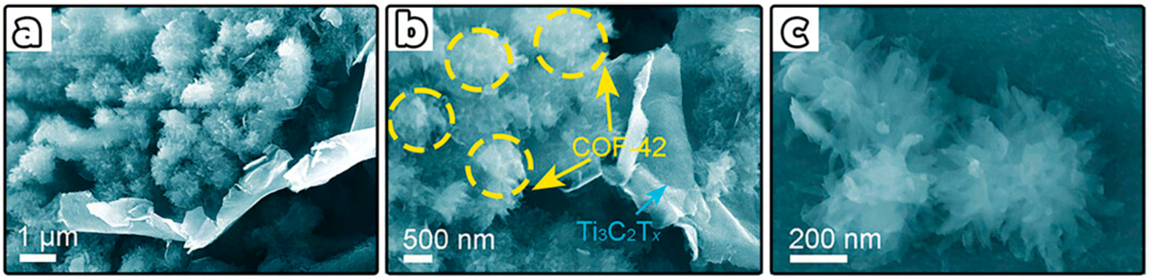

Fig. 5. SEM images with different magnifications of the COF@$Ti_3C_2T_x$ heteroconjugate prepared by the growth of COF (made of 2,5-diethoxyterephthalohydrazide and 1,3,5-triformylbenzene) on the surface of $Ti_3C_2T_x$ [105].

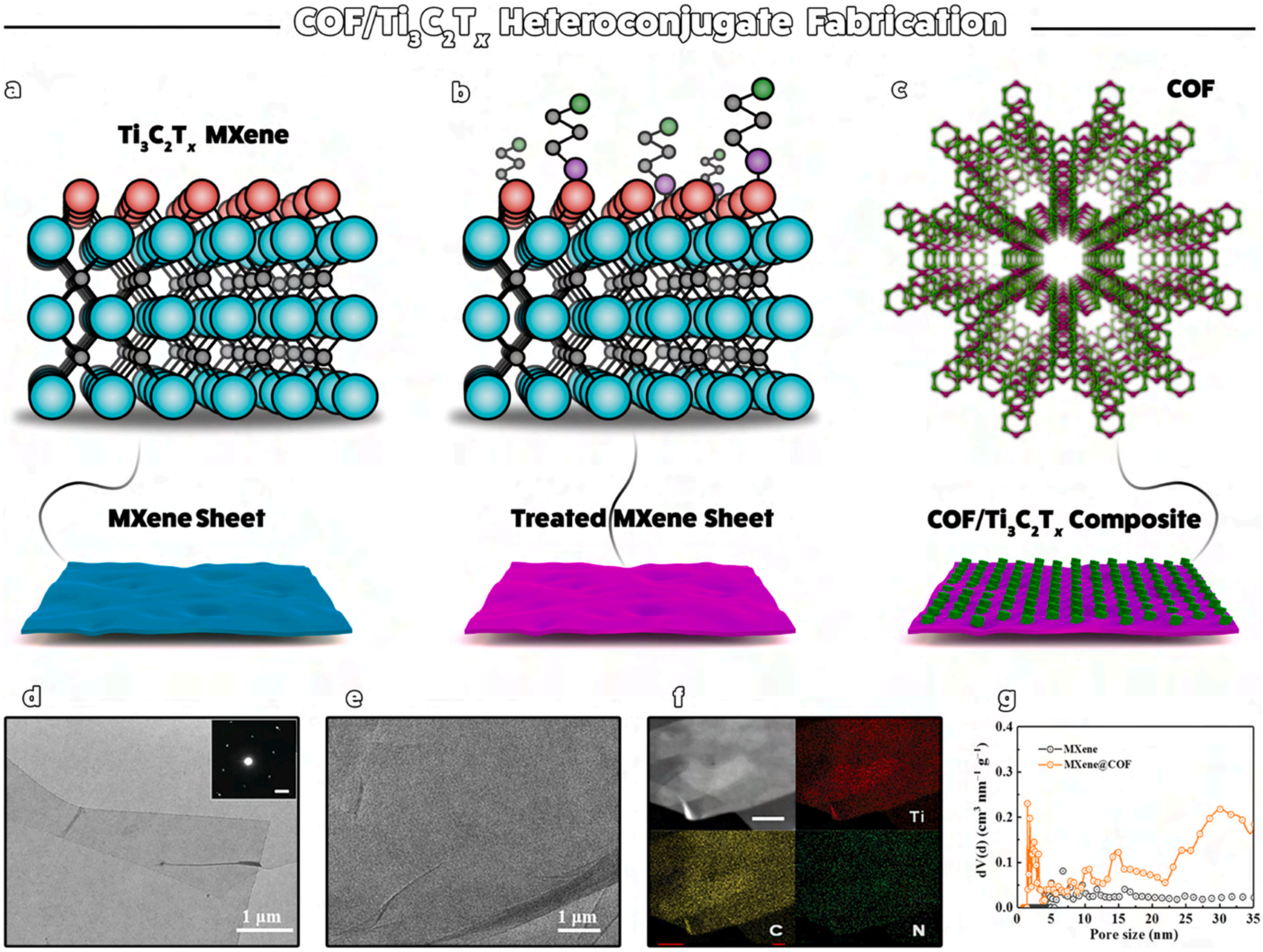

Fig. 6. (a) The schematic process for fabricating a COF@$Ti_3C_2T_x$ heteroconjugate. The transmission electron microscopy (TEM) image of (b) $Ti_3C_2T_x$ nanosheets and (c) COF@MXene heteroconjugate. (d) Energy dispersive spectroscopy (EDS) mapping images of the COF@MXene heteroconjugate. (e) The pore size distribution of the COF@MXene heteroconjugate[106]. Reproduced with Permission from Wiley, 2021.

photocatalysis, the fast charge recombination dramatically reduces the photocatalytic activity of pristine COFs. Hybridization is an effective strategy to increase the charge-carrier separation in photo-redox processes [118]. There are many reports on improving photocatalytic activity of COFs by its hybridization with other nanomaterials [119–121]. The covalent integration of MXenes into COFs provides a platform for effective visible-light-induced photocatalytic H_2 evolution from water using Pt-based catalysts [99]. A heteroconjugation of NH_2–$Ti_3C_2T_x$ MXene with a COF (made of 2,4,6-trihydroxybenzene-1,3,5-tricarbaldehyde and *p*-phenylenediamine) showed that the incorporation of MXenes does not alter the band gap of the COFs (Fig. 8a) [99].

In contrast to the pristine COFs, the photoluminescence (PL) quenching was observed for the COF@MXene composite (Fig. 8b). The PL quenching and increased average emission lifetime for the COF@MXene composite (1.307 ns) compared to the pure COFs (0.950 ns) indicating that the creation of a charge transfer channel between MXenes and the COFs effectively suppresses the charge recombination and interfacial charge transfer through the COF@MXene heterojunction. Time-resolved transient absorption and electrochemical impedance spectroscopy further confirmed the inhibition of charge recombination. Fig. 8c shows that H_2 production by covalently conjugated COF@NH_2-$Ti_3C_2T_x$ MXene hybrid, which was much higher compared with the pristine COFs or physically mixed COFs/NH_2-$Ti_3C_2T_x$ and the *in situ* prepared COF@$Ti_3C_2T_x$ MXene composite. This indicates that the covalent bonding between NH_2-$Ti_3C_2T_x$ MXenes and the COFs is critical in increasing the photocatalytic activity. The mechanism of the water reduction is depicted in Fig. 8d. The visible light irradiation leads to the transfer of electrons in the $HOMO_{(ground\ state)}$ of COFs to $HOMO_{ex}$. The transferred electrons in $HOMO_{ex}$ are then transferred to NH_2-$Ti_3C_2T_x$ MXene via the covalent linkage between the COFs and NH_2-$Ti_3C_2T_x$ MXenes due to its lower Fermi (E_F) level position and excellent metal-like electrical conductivity. These separated electrons via cascade charge transfer result in the continual reduction of water into H_2 with the assistance of the Pt co-catalyst. COFs and Pt, respectively, act as the photosensitizer and co-catalyst, whereas MXene acts as an electron sink and conductor. Importantly, the photocatalytic activity of COF@MXene hybrid remained unchanged after 6 cycles during duration of 30 h (Fig. 8e). The PXRD patterns and SEM morphology COF@MXene were almost the same before and after 6 cycles of photocatalysis. These results indicates that the prepared COF@MXene offer excellent photocatalytic activity, recyclability, and structural stability.

Doping COF@MXene hybrid with semiconductors (e.g., Si, ZnO, and TiO_2), metal nanoparticles (e.g., Ag, Au, and Pt), and metal oxides (e.g., Al_2O_3, Fe_3O_4, and ZrO_2) can further increase the photocatalytic activity via facilitating the charge separation and inhibition of the charge recombination. $ZnIn_2S_4$ (ZIS) semiconductor nanosheets with high stability, suitable band gap, non-toxicity, high visible light absorption, and excellent electrical and optical properties have been widely used in photocatalytic H_2 evolution [122]. Therefore, incorporating ZIS into COF@MXene provides a photocatalyst with improved performance

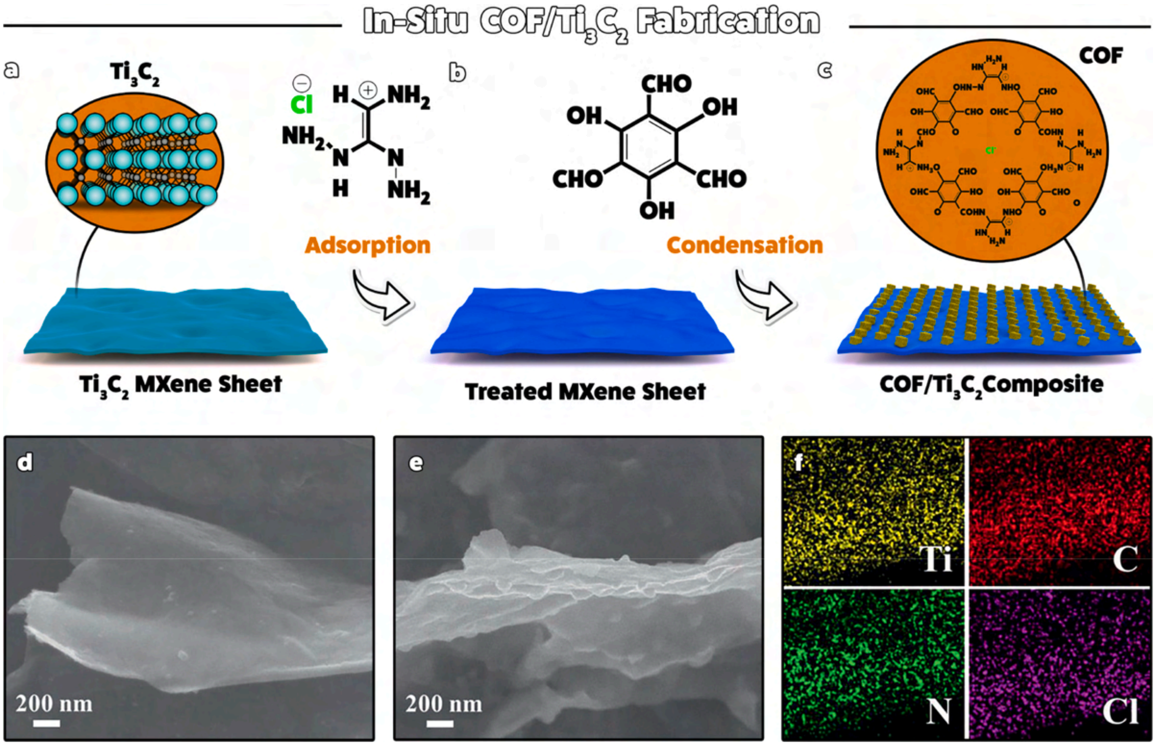

Fig. 7. The schematic description for the *in-situ* preparation of a COF@MXenes. SEM images of (b) MXenes and (c) COF@MXene hybrid. (d) The elemental mapping of the COF@MXene hybrid[107]. Reproduced with Permission from Wiley, 2021.

[108]. Electrochemical impedance spectroscopy (EIS) showed that the *in situ* prepared ZIS@COF@$Ti_3C_2T_x$ MXene composite (COF is made of 1,3,5-triformylphloroglucinol and tris(4-aminophenyl)amine) has a smaller half-circle than the pristine COF, ZIS, and COF@ZIS, indicating its lower charge transfer resistance and higher electron transfer efficiency (Fig. 9a). Under visible-light irradiation ($\lambda > 420$ nm), the H_2 production rate for COF@ZIS was 2.46 mmol g^{-1} h^{-1}, which increased to 4.01 mmol g^{-1} h^{-1} for ZIS@COF@MXene containing 2 wt% $Ti_3C_2T_x$ MXene as the co-catalyst (Fig. 9b). Notably, after 6 cycles the photocatalytic activity of ZIS@COF@MXene showed a negligible decline (Fig. 9c), indicating its excellent photocatalytic stability. In this photocatalyst, ZIS and COFs act, respectively, as reduction-type and oxidation-type photocatalysts (Fig. 9d). Therefore, the electron transfer from ZIS to COFs happens spontaneously (Fig. 9e) and generate an interfacial electric field. The visible light irradiation excites the electrons in the COFs to the conduction band (CB) and then transfers them into the valence band (VB) of ZIS. At the same time, the electrons in ZIS are excited to its CB and then transferred to MXene (Fig. 9f). The photogenerated electrons and holes induce H_2 evolution and ascorbic acid oxidation.

The CO_2 reduction process is of high importance for CO_2 utilization and for reducing greenhouse gases. Among different methods for the CO_2 reduction, the enzymatic CO_2 reduction has the advantages of performing under mild reaction conditions and high selectivity. One of the main methods for CO_2 reduction is its selective conversion into formate using formate dehydrogenase (FDH) enzyme [123,124]. The electron transfer in this process is facilitated by the nicotinamide adenine dinucleotide (NADH) coenzyme that is the active site in FDH. However, the high cost of NADH highlights the importance of the in-situ regeneration of NADH during the reduction process. The combination of porous structure and adjustable band gap in COFs with the excellent conductivity of MXene enables the easy transfer of photogenerated charges and regeneration of NADH. Accordingly, utilization of the Ti_3C_2/COF-367 heterostructure as a photocatalyst showed a regeneration yield of 83.38 % for NADH due to its fast charge separation and transfer [110]. A HCOOH production rate of 1.88 mmol g^{-1} h^{-1} with 100 % selectivity was reported. Since various types of noble metals have been used in NADH regeneration [125,126], therefore, doping noble metals in the COF@MXene structures can further improve the NADH reaeration rate. One of the main metal complexes that have been used in this context is pentamethylcyclopentadienyl rhodium 2,2′-bipyridin ($[Cp^*Rh(bpy)H_2O]^{2+}$) catalyst. Accordingly, Wei et al. reported that utilization of COF@NH_2–$Ti_3C_2T_x$ heteroconjugate (COF made from 2,4,6-tris(4-formylphenoxy)-1,3,5-triazine and 1,4-phenylenediacetonitrile) as a photocatalyst yield an NADH regeneration rate of 95 % and 46 % in 30 min, with and without $[Cp^*Rh(bpy)(H_2O)]^{2+}$, respectively [111]. Importantly, the turnover frequency (TOF) for the NADH regeneration reaction by COF@MXene catalyst in the presence and absence of Rh-complex was 4.05 and 4.90 times higher than that of pure COF indicating the synergistic effects between COF and MXene. The formate generation rate by the COF@MXene photocatalyst in the absence and presence of Rh-complex was around 543 and 2380 μmol g^{-1} h^{-1}. Similarly, another COF/NH_2-$Ti_3C_2T_x$ heteroconjugate (COF made of 4,4′,4″-(1,3,5-triazine-2,4,6-triyl)tribenzene and 2,6-pyridinedicarbaldehyde) in the presence of $[Cp^*Rh(bpy)(H_2O)]^{2+}$ showed a 95.0 % NAADH regeneration rate with 88 % selectivity toward production of 1,5-NADH over 1,6-NADH [112]. The formate production rate by this catalyst was 2137.7 μmol g^{-1} h^{-1}.

The photocatalytic activity of COF@MXene composites under visible light could be further increased by surface-anchoring with Ag NPs [113] and Cu_2O NPs [114]. The COFs, MXenes, and Ag or Cu_2O NPs act, respectively, as the photocatalyst, co-catalyst, and electronic medium. The absorption of visible light by COFs, as an *n*-type semiconductor, produces electron-hole pairs, which lead to the generation of reactive oxygen species (ROS) that can induce oxidative stress in microbial cells. Combining COF with MXenes and Ag NPs increases the lifetime of the photogenerated carriers and improves the electron-hole separation which lead to the generation of more ROS. The antibacterial activity of pristine COFs, COF@MXene and Ag@COF@MXene against *S. aureus* and *P. aeruginosa* was around < 60 %, > 70 %, and > 99 %, respectively

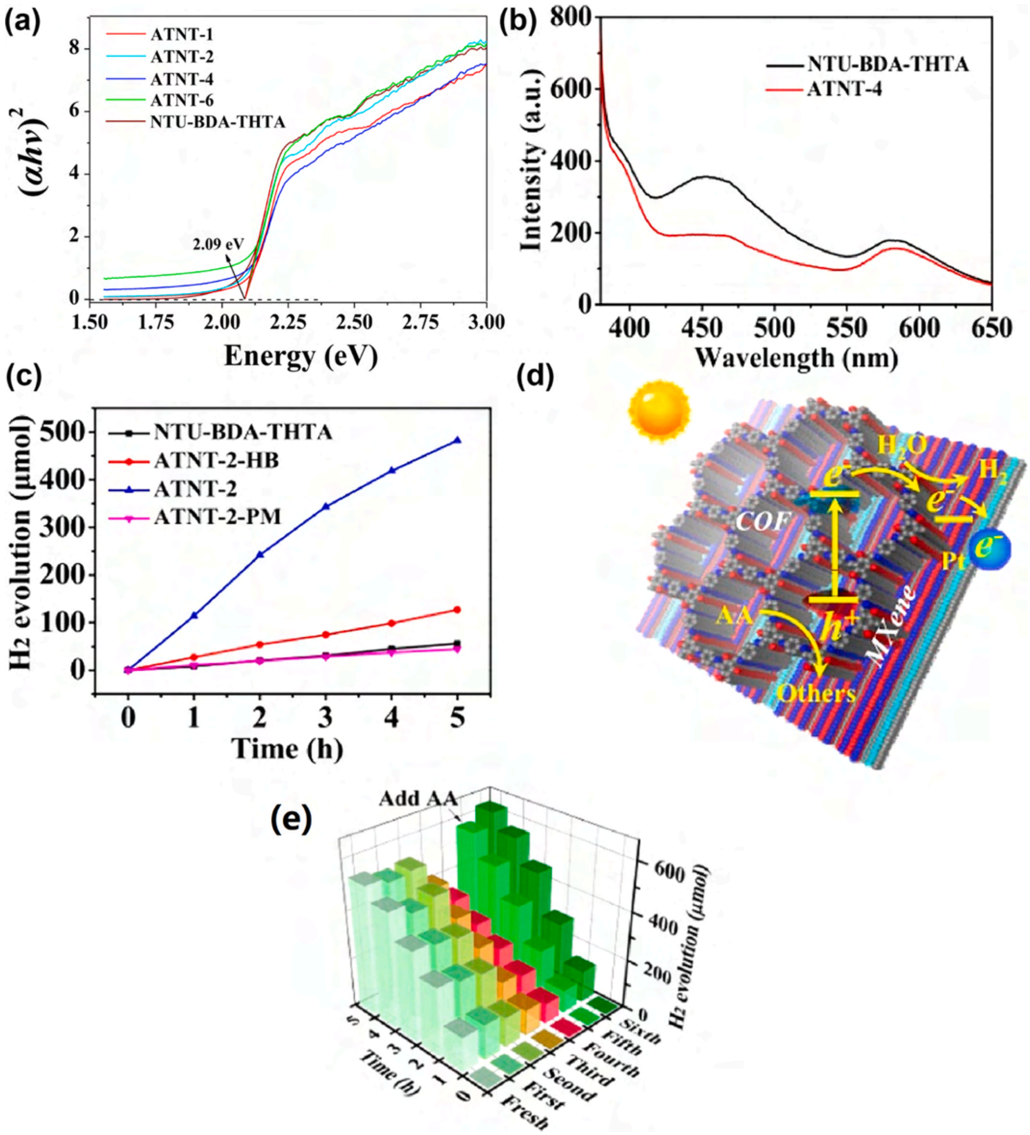

Fig. 8. (a) The band-gap energy spectra of COFs and COF@NH_2-$Ti_3C_2T_x$ MXene conjugate (ATNT), (In ATNT1, 2, 4, and 6, the weight ratio of COF:NH_2-$Ti_3C_2T_x$ is 8:1, 8:2, 8:4, and 8:6, respectively). (b) The steady-state photoluminescent spectra of the neat COF and COF:NH_2-$Ti_3C_2T_x$ composite. (c) The compassion of the photocatalytic H_2 evolution from water using different platforms (ATNT-2-HB: the in situ formed COF in the presence of $Ti_3C_2T_x$; ATNT-2-PM: a physical mixture of the COF with NH_2-$Ti_3C_2T_x$). (d) The mechanism for photocatalysis with the COF@NH_2-$Ti_3C_2T_x$ MXene conjugate. (e) Recyclability of ATNT-4 for the generation of H_2 during 30 h [99]. Reproduced with Permission from American Chemical Society, 2020.

(Fig. 10a) [113]. Indeed, the lifetime of the photogenerated charge carriers by COFs, COF@MXene, and Ag@COF@MXene were 0.11, 0.16, and 0.34 ns, respectively. Notably, the photocurrent intensity of Ag@COF@MXene was higher than that of COFs and COF@MXene, and the performance also remained unchanged after 500 cycles (Fig. 10b,c). The photocatalytic mechanism for the ROS generation by Ag@COF@MXene is depicted in Fig. 10d. As an electron receiver, MXenes, with a band gap close to zero, prevent the electrons from returning to the ground state and reduce the charge recombination rate. Also, Ag NPs act as an electron absorber and form a barrier to inhibit the charge recombination. Therefore, the excited electrons in COFs are transferred into Ag NPs and MXenes which lead to the significant improvement in the electron-hole separation.

Photocatalytic reduction of soluble U(VI) to insoluble U(IV) is an excellent approach for preventing uranium contamination [127]. Additionally, due to the porous and tunable structures, COFs have been widely used to extract U(VI) [128]. However, the poor π-electron delocalization in COFs reduces their photocatalytic activity. Heteroconjugation of COFs (made of 4,4′,4′′-(benzene-1,3,5-triyltris (ethyne-2,1-diyl))tris(2-hydroxybenzaldehyde) and 2,2′-bipyridine-5, 5′-diamine) with NH_2-$Ti_3C_2T_x$ MXene provides an excellent platform for U(VI) photo-reduction [129]. The conduction band potentials (E_{CB}) of the COFs and COF@MXene were around −0.92 and −1.21 eV (*vs.* standard hydrogen electrode, NHE) due to the transfer of photo-generated electrons from the COF to the MXenes in the COF@MXene heterostructure (Fig. 11a). Also, the valence band potentials (E_{VB}) for the COFs and COF@MXene were around 1.46 and 1.13 eV (vs NHE), respectively. It shows that the reduction potential of the COF@MXene is more negative than that of U(VI)/U(IV) (0.41 eV) indicating the capability of this composite to be used for photo-reduction of U(VI). The transient photocurrent response of the COF@MXene was bigger than the pristine COFs which imply on more electron accumulation due to the better electron-hole separation (Fig. 11b). Furthermore, the weaker intensity of the steady-state photoluminescence (PL) of the COF@MXene than the pristine COFs confirms its slower charge recombination (Fig. 11c). The weaker charge transfer impedance of the COF@MXene

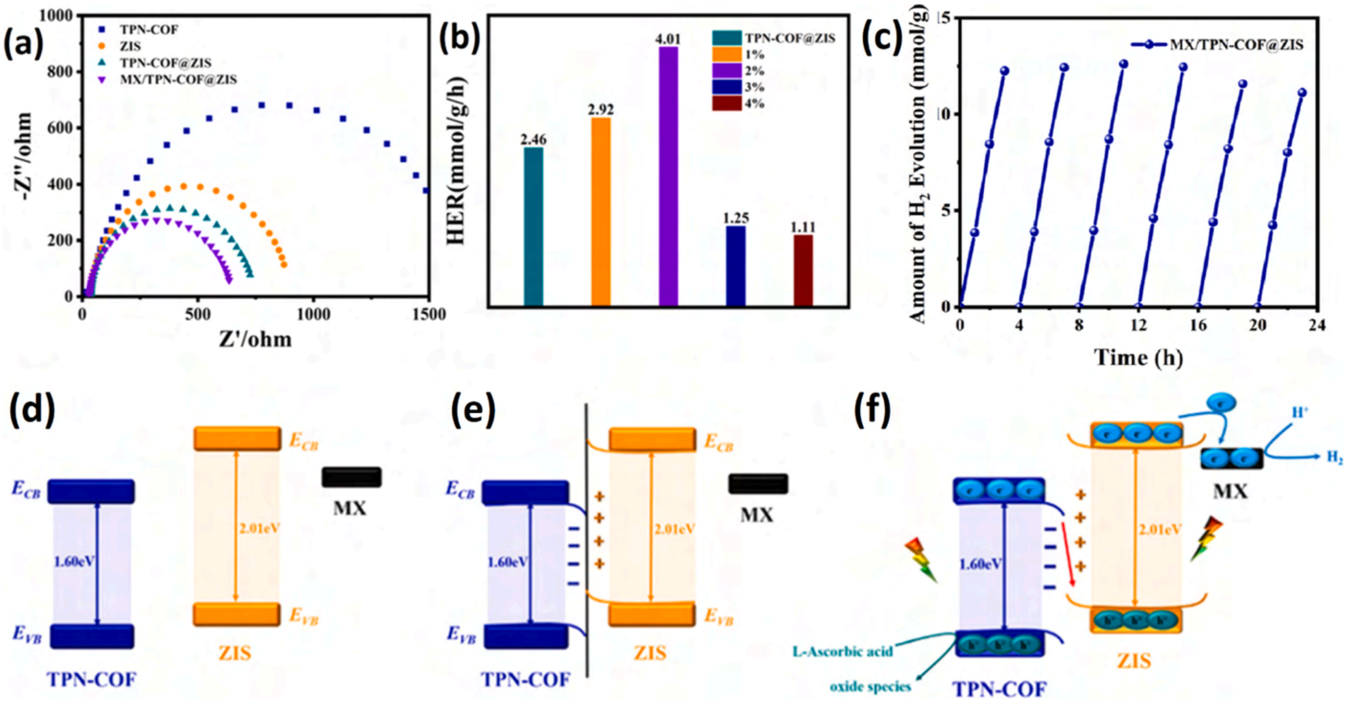

Fig. 9. (a) Electrochemical impedance spectroscopy (EIS) Nyquist plots of COFs, ZIS, COF@ZIS, and ZIS@COF@MXene catalysts. (b) The electrocatalytic hydrogen evolution reaction (HER) COF@ZIS and ZIS@COF@MXene catalyst bearing different contents (1–4 wt%) of MXenes. (c) Photocatalytic durability assessment of ZIS@COF@MXene catalyst. The charge transfer mechanism in ZIS@COF@MXene catalyst (d) before contact, (e) after contact, and (f) under visible light illumination [108]. Reproduced with Permission from Wiley, 2023.

than the COFs was realized from its smaller semicircular arc radius in the Nyquist plot (Fig. 11d). The pristine MXenes showed no photoreduction activity toward U(VI) and the adsorption of U(VI) in dark or light was the same. However, the adsorption by the COFs and COF@MXene was increased in the presence of light, with the highest adsorption capacity of 1557 mg g^{-1} (pH 5) for the COF@MXene under simulated sunlight (Fig. 11e). Indeed, the presence of the alkyne groups in the COFs improves the charge transfer and increases light absorption. At the same time, the presence of MXene reduces the hydrophobicity of COFs, which facilitates the interaction with U(VI). The photo-reduction kinetics of U(VI) by the COF@MXene were more than 3 and 14 times faster than those for the pristine COFs and MXenes, respectively (Fig. 11f). The catalyst showed acceptable stability and recyclability so that the removal rate of U(VI) reduced slightly from 97.8 % to 91.9 % after five photoreduction cycles.

5.1.2. COF@MXene Hybrids as Electrocatalysts

In another area of catalysis, MXene@COF hybrids are utilized as cathodes for electrocatalytic H_2 evolution through water electrolysis. Although MXenes exhibit favorable activity in the hydrogen evolution reaction (HER), the performance is hindered by the accumulation of generated H_2 on the active site of MXenes. Creating defects in the MXenes structure and increasing the porosity can accelerate the H_2 diffusion reaction kinetics. Coating a COF@$Ti_3C_2T_x$ composite (COF made of 2,5-diethoxyterephthalohydrazide and 1,3,5-triformylbenzene) on the surface of a glassy carbon electrode (GCE) and utilizing it as a cathode in the HER showed that the COF(40 %)/$Ti_3C_2T_x$ MXene electrode has a much better performance than that of the pristine COFs and MXene electrodes [105]. The linear sweep voltammetry (LSV) showed that the onset potential of the COF@MXene electrode is 19 mV (vs. RHE) with no changes after 2000 cycles, which is much smaller than that for the pristine COFs (205 mV) and MXenes (276 mV) electrodes. Additionally, it demonstrated the lowest overpotential of 72 mV at 10 mA cm^{-2} (close to the commercial Pt/C electrode) is much smaller than that of the pristine COFs and MXene electrodes (Fig. 12a). In addition, the kinetics of electrodes in HER shown in Tafel plots demonstrated a Tafel slope of 50 mV dec^{-1} for the COF(40 %)@MXene electrode (close to the Pt/C electrode), which is smaller than that for the pristine COFs and MXene electrodes (Fig. 12b). Moreover, the performance of the COF@MXene electrode is much better than many of the other MXenes-based hybrid electrodes (Fig. 12c). The double-layer capacitance (C_{dl}) for the COF@MXene was 30.0 mF cm^{-2}, which is much larger than that for the pristine COFs (2.7 mF cm^{-2}) and MXenes (1.5 mF cm^{-2}). This shows that the COF@MXene has a larger electrochemically active surface area (ECSA) than the individual COFs and MXenes. Also, the electrochemical performance of the electrode remained unchanged for a continuous use of 24 h. The LSV curve using the COF (40 %)/MXene electrode after 2000 cycles showed almost no changes (Fig. 12d) indicating its capability in sustainable electrocatalytic H_2 evolution during the HER process.

To further improve the catalytic activity of MXene/COF composites, Zong et al. developed a Ni-doped Ti_3CNT_x@COF hybrid (NMXC) for improving the diffusion of H_2 and increasing the HER yield [115]. Doping Ni can generate defects in MXenes and increase their catalytic activity. The obtained NMXC was used as a cathode for water electrolysis. Evaluation of the HER by linear sweep voltammetry (LSV) at 10 mA cm^{-2} showed that the pristine MXene has an overpotential of 398 mV at pH = 0 which was reduced to 164 mV by incorporation of 0.3 % Ni and COFs ($N_{0.3}$MXC). Additionally, the C_{dl} for $N_{0.3}$MXC was higher (102.2 mF cm^{-2}) than other electrodes that indicates its lower inherent resistance (R_s). Furthermore, the $N_{0.3}$MXC electrode demonstrated the most-negligible charge-transfer impedance (R_{ct}) with a value of 6.8 Ω. Evaluation the long-term stability of this catalyst showed a slight decline in the current density (7.8 % reduction) after 18 h of operation. The mechanisms for the HER under acidic and alkaline conditions are illustrated in Fig. 13a. In acidic conditions, protons are adsorbed on the catalyst surface and combined to generate H_2 whereas under alkaline conditions, two H_2O molecules lose one H_2 at the catalyst's active site. The evaluation of the chemical reactivity of different sites on the $N_{0.3}$MXC catalyst (Fig. 13b) showed that the change in the

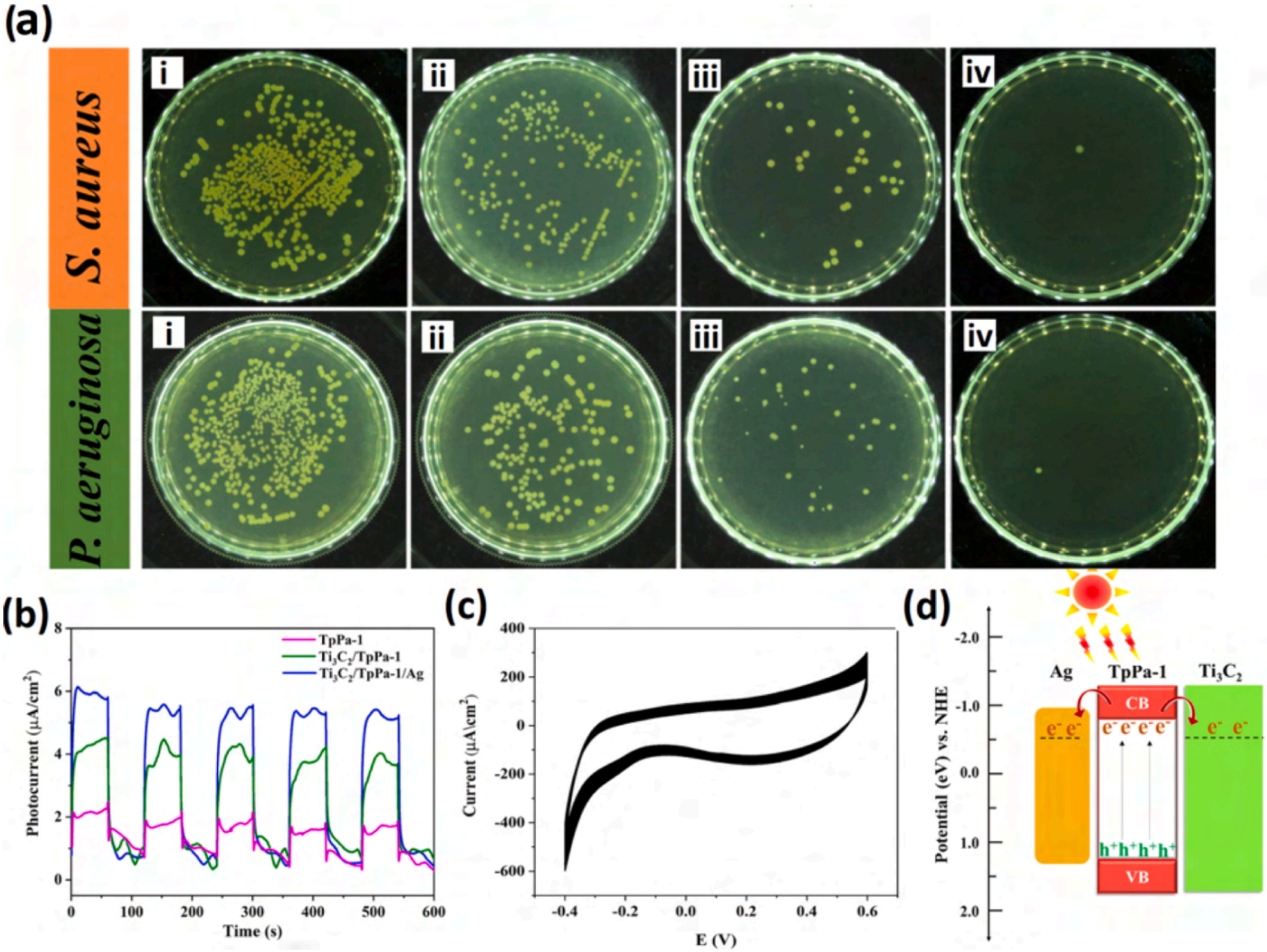

Fig. 10. (a) Images of agar plates of antibacterial properties of (i) control (blank), (ii) COFs, (iii) COF@$Ti_3C_2T_x$ MXene, and (iv) Ag@COF@$Ti_3C_2T_x$ MXene composites against *S. aureus* and *P. aeruginosa*. (b) Photocurrent curves of COF, COF@$Ti_3C_2T_x$ MXene, and Ag@COF@$Ti_3C_2T_x$ MXene (c) Polarization curves of the COFs, COF@$Ti_3C_2T_x$ MXene, and Ag@COF@$Ti_3C_2T_x$ MXene before and after 500 CV cycles. (d) The photocatalytic antibacterial mechanism of Ag@COF@$Ti_3C_2T_x$ MXene composite[113]. Reproduced with Permission from Elsevier, 2022.

Gibbs free energy (ΔG) at Ni-doped sites is negligible (0.06 eV) (Fig. 13c) indicating its highest reactivity in the HER process. Indeed, the $|\Delta G_{H^*}|$ of the Ni-doped sites was even smaller than that of the Pt ($|\Delta G_{H^*}| = 0.09$ eV). This clearly proves the important role of Ni in improving the HER reactivity of MXene/COF electrodes.

Electrocatalytic nitrogen reduction reaction (NRR) is an energy-efficient and environmentally friendly method for converting N_2 to ammonia [130,131]. Both COFs [132] and MXenes [133] have been used in NRR applications. Meanwhile, Fe represents a prime non-noble metal choice for transforming N_2 to NH_3. Additionally, suppressing the competitive HER can be achieved by hydrophobizing the catalyst which repels water molecules and prevents HER. Therefore, utilizing superhydrophobic catalysts based on Fe-doped COF@MXene composites can provide synergistic effects with stronger performances. Accordingly, a superhydrophobic perfluorinated Fe-doped COF@NH_2-$Ti_3C_2T_x$ MXene composite (COF made of 2,2′-bipyridine-5,5′-diamine and 1,3,5-triformylphloroglucinol) was developed as an efficient electrocatalyst for the NRR process [116]. This catalyst exhibited stronger performance than similar catalysts without one of its components (Fig. 14a). An NH_3 production yield of 41.8 μg h^{-1} $mg_{cat.}^{-1}$ and a Faradaic efficiency of 43.1 % at −0.5 V versus the reversible hydrogen electrode (RHE) were achieved. Indeed, the interaction between Fe 3d and N 2p orbitals improves the NRR electrocatalytic catalytic. Additionally, the C_{dl} for MXenes, Fe/COFs, and Fe/COFs@MXene were around 3.9, 9.4, and 18.5 mF cm^{-2}, respectively, indicating the critical role of MXenes in facilitating the electrolyte access to active catalytic surfaces. The performance of this catalyst was higher than many of the reported Fe-based catalysts (Fig. 14b). Additionally, the hydrophobicity improved the N_2-to-NH_3 conversion by suppressing the competitive HER via inhibiting water accessibility to active sites (Fig. 14c). Additionally, the assessment of the electrocatalytic stability of this hydrophobized Fe/COF@MXene at −0.5 V relative to RHE showed that the Faradaic efficiency and NH_3 production rate remained unchanged during 2 h of operation and after 10 cycles (Fig. 14d). This indicates the high stability of the catalyst during the NRR process.

Direct methanol fuel cells (DMFCs) are among the highly efficient portable electrical devices due to their excellent energy conversion efficiency and wide operating temperature range [134,135]. One of the drawbacks of this system is the slow kinetics of the methanol oxidation reaction (MOR) at the anode. Therefore, fabrication of new anodic materials with better oxidation performance is in high demand. Palladium-based anode is highly utilized in DMFCs. However, applying a pure Pd-based anode increases the cost significantly. Therefore, doing Pd into the materials with high surface area can be used as an alternative to reduce the cost. Accordingly, Yue et al. utilized confined Pd nanocrystals within COF@MXene nanoarchitectures as an anode for the methanol oxidation [117]. This electrode showed an electrochemically active surface area (ECSA) of 112.1 m^2 g^{-1}, a mass activity of

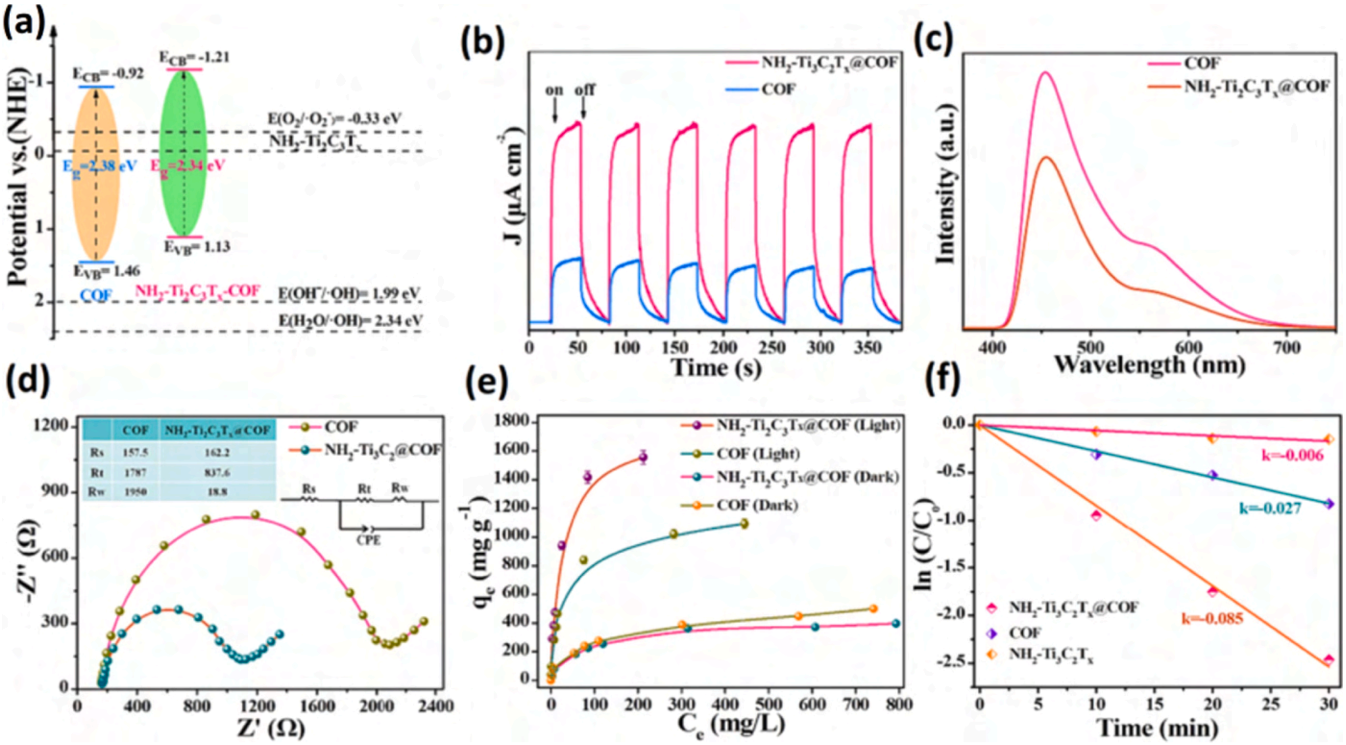

Fig. 11. (a) The band-structure profile for MXenes and COF@MXene. (b) The transient photocurrent responses. (c) Photoluminescence spectra. (d) Electrochemical impedance spectroscopy Nyquist spectra of COFs and COF@MXene. (e) The adsorption isotherms of U(VI) by COFs and COF@MXene in dark and under simulated sunlight at pH 5.0. (f) The kinetics of U(VI) photo-reduction by COFs, MXenes, and COF@MXene[129]. Reproduced with Permission from Elsevier, 2023.

1478.4 mA mg^{-1}, outstanding CO resistance, and long-term durability during the methanol electrooxidation process. The methanol electrooxidation using this electrode as an anode in a mixed electrolyte (0.5 mol L^{-1} NaOH and 1 mol L^{-1} CH_3OH) exhibited a current density of 1478.4 mA mg^{-1} (Fig. 15a). However, other Pd-based electrodes (such as Pd/MXene, Pd/rGO, Pd/CNT, and Pd/C) exhibited weaker current densities in the range of 251–644 mA mg^{-1} (Fig. 15b). Additionally, it showed a remarkably higher specific activity (1.32 mA cm^{-2}) compared to other Pd-based anodes (Fig. 15c). Furthermore, the LSV assessment showed that the required anodic voltage for starting the methanol electrooxidation reaction for Pd/COF@MXene electrode was 136 mV dec^{-1} whereas the value for the other Pd-based electrodes was in the range of 193–256 mV dec^{-1} (Fig. 15d,e). Evaluating the stability of different electrodes at a specific potential of 0.85 V showed that the methanol electrooxidation current is declining due to the gradual adsorption of intermediate products on the active sites of the electrodes (Fig. 15f). Nevertheless, the stability of the Pd/COF@MXene electrode was much higher than other Pd-based electrodes.

5.2. Advancing Energy Storage with COF@MXene Composites

5.2.1. COF@MXene hybrids in rechargeable batteries

The high surface area and highly porous structure of COFs along with the high conductivity and ease of processing of MXenes, make COF@MXene hybrid composites excellent materials for the fabrication of electrodes in energy storage materials including rechargeable batteries and supercapacitors. Table S5 presents a detailed overview of the performance of COF@MXene hybrids in energy storage applications.

While pure MXenes are useful in Li-S batteries, their tendency to restack significantly decrease their specific surface area. Incorporation of MXenes into porous materials can address this issue. The COF@MXene hybrids have been utilized in Li-S batteries as sulfur hosts in the cathode, lithium hosts in the anode, and modifiers of the separator. One of the main problems of Li-S batteries is the so-called "shuttle effect." It is caused by the dissolution and diffusion of lithium polysulfides between the anode and cathode, resulting in weak cycling stability and corrosion. Therefore, developing suitable sulfur hosts with an effective shuttle effect inhibition is in high demand [136,137]. The abundant lipophilic N sites in the COF and sulfurophilic Ti sites in $Ti_3C_2T_x$ MXene generate strong dual sites for chemical interactions between the host and polysulfides which can effectively suppress the shuttle effect. Accordingly, a composite with 76 wt% sulfur was obtained by mixing a COF@$Ti_3C_2T_x$ MXene hetero-conjugate (COF made of 1,4-dicyanobenzene) with sulfur and heating at 155 °C under vacuum [102]. The effective entrance of sulfur in pores of the COF@$Ti_3C_2T_x$ composite is proved by the significant reduction of specific surface area from 318 m^2 g^{-1} to 9 m^2 g^{-1} upon sulfur mixing. The S@COF@$Ti_3C_2T_x$ MXene cathode exhibited a high reversible capacity of 1441 mA h g^{-1} at 0.2 C and excellent cycling stability of 1000 cycles at 1 C with a negligible (≈ 0.01 %) capacity decay rate per cycle. COF@MXene composites prepared by physical mixing can also be used as hosts for the sulfur cathode. A flexible and binder-free 3D porous COF-derived carbon film in combination with $Ti_3C_2T_x$ MXene was used as a host for sulfur cathode in Li-S batteries to render the conductivity and restrict the LiPSs. The cathode was fabricated in three steps including the carbonization of the COFs (composed of 1,3,5-triformylbenzene + tris(4-aminophenyl) amine) followed by loading with sulfur via the melt diffusion method, and finally, vacuum filtration of a mixed dispersion of MXenes and carbonized-COF/sulfur [138]. The corresponding battery showed a good discharge capacity of 584 mAh g^{-1} after 100 cycles.

Another problem of Li-S batteries is inhomogeneity in the ionic distribution of lithium around the Li anode surface through the electromigration pathway which leads to internal short circuits due to uneven Li nucleation and dendrite growth [139]. The main reasons for Li deposition are mass transfer and electro-reaction-controlled overpotential. Utilizing a 3D conductive host can improve mass transfer, reduce the current density, and inhibit charge accumulation [140]. Additionally, the presence of lithiophilic units is essential to facilitate

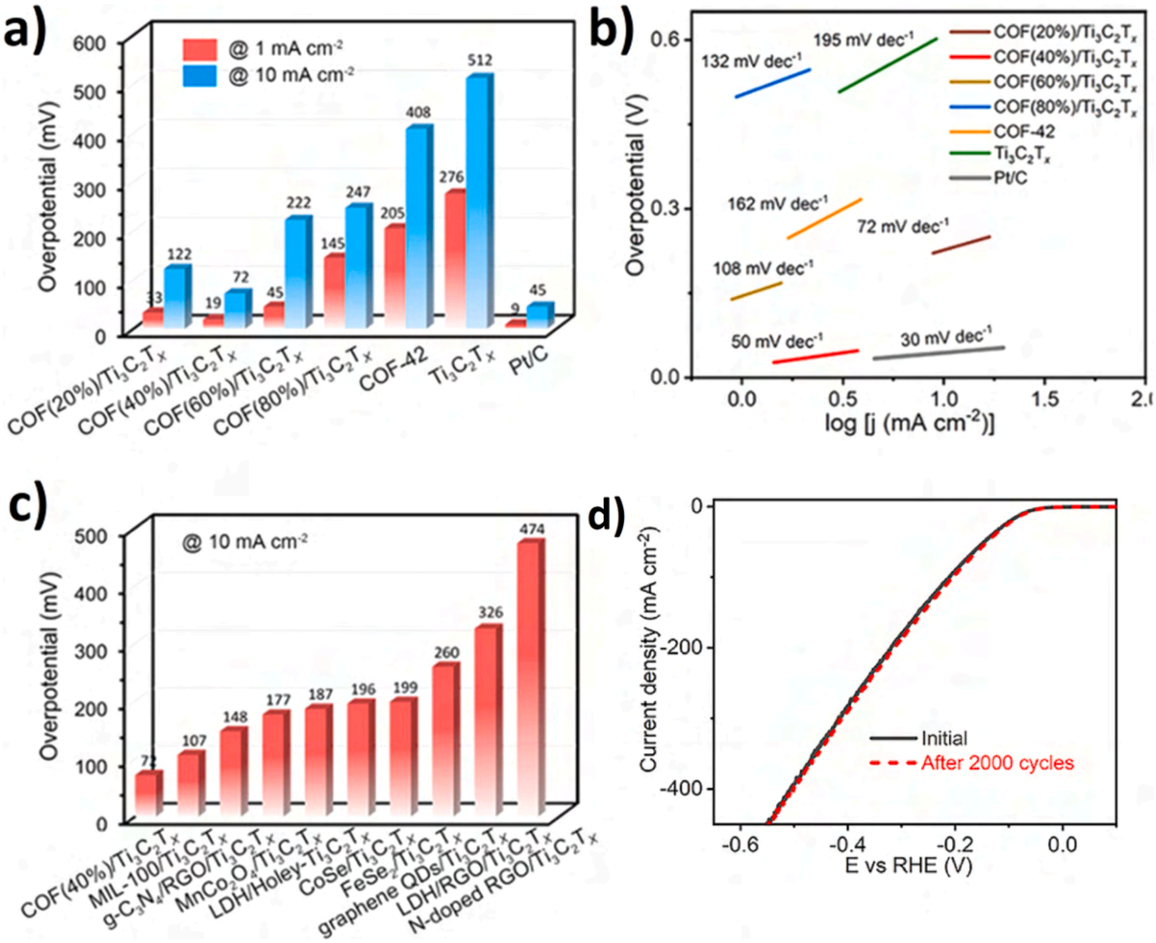

Fig. 12. Comparison of the HER performance of different electrodes by determining (a) histograms of required overpotentials and (b) Tafel slope in a 0.5 M H_2SO_4 solution. (c) Comparison of the overpotentials of the COF@MXene at 10 mA cm^{-2} with other MXenes-based composite electrodes. (d) Assessing the cycling ability and long-term stability of the COF (40 %)/MXene electrode [105]. Reproduced with Permission from Wiley, 2024.

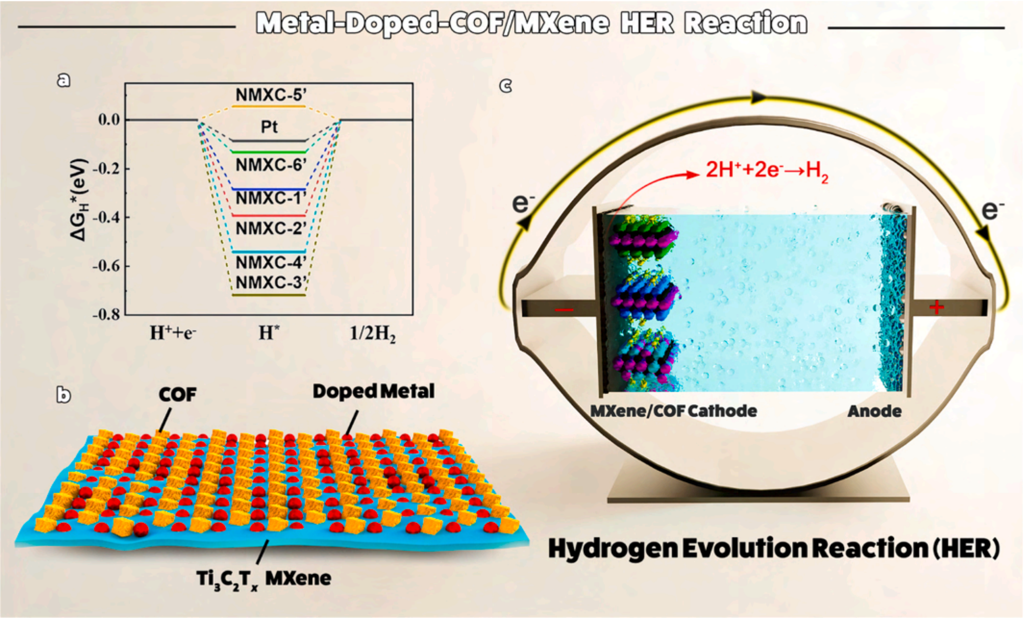

Fig. 13. (a) HER mechanism from the surface of the Ni-doped MXene@COF (NMXC) cathode in acidic and alkaline environments. (b) The possible different hydrogen adsorption sites on the surface of the NMXC cathode. (c) The Gibbs free energy change (ΔG) of hydrogen adsorption on different sites of the NMXC cathode [115]. Reproduced with permission from American Chemical Society, 2023.

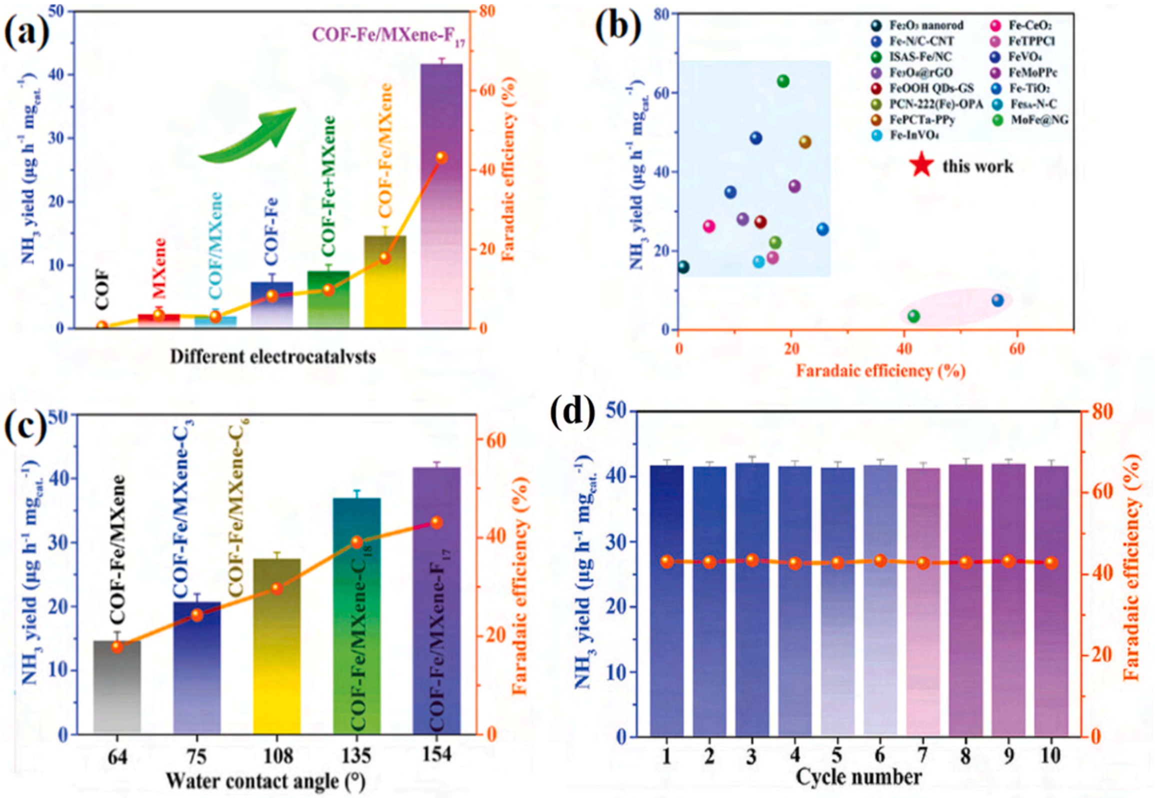

Fig. 14. Electrocatalytic NRR performances of (a) the pristine COFs, MXenes, COF@MXene, Fe/COFs, physically mixed Fe/COFs and MXenes, Fe/COF@MXene, and the hydrophobized Fe/COF@MXene, (b) different Fe-based catalysts, (c) hydrophobized Fe/COF@MXene catalysts with different alkyl thiols as hydrophobic agents, and (d) the hydrophobized Fe/COF@MXene for ten sequential cycles. [116]. Reproduced with Permission from Wiley, 2023.

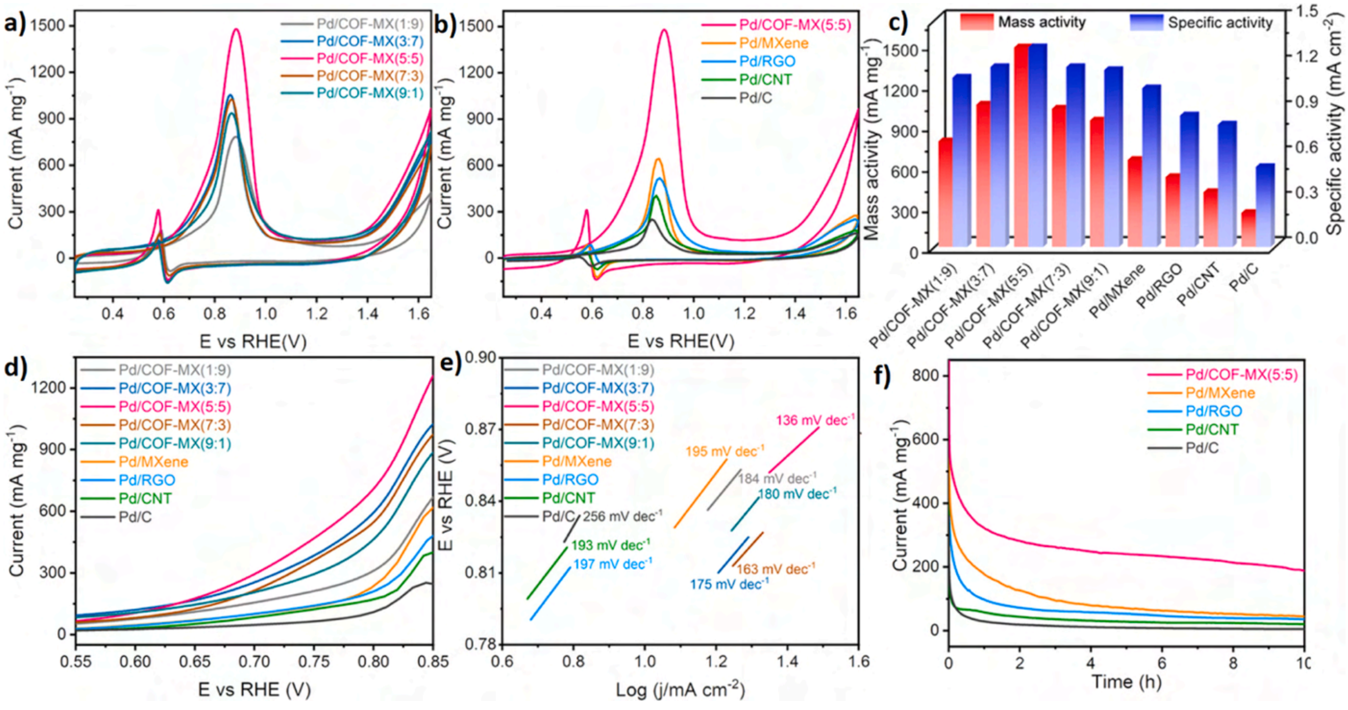

Fig. 15. CV results of (a) Pd/COF@MXene electrodes with different COF:MXene ratios and (b) other Pd-based electrodes in 0.5 mol L^{-1} NaOH with 1 mol L^{-1} CH_3OH. (c) Mass activity and specific activity of different electrodes (d) LSV and (e) Tafel graph of different electrodes. (f) The current-time data of different electrodes in 0.5 mol L^{-1} NaOH with 1 mol L^{-1} CH_3OH [117]. Reproduced with permission from American Chemical Society, 2025.

Li^+ diffusion and reduce nucleation overpotentials which prevent Li nucleation and dendrite growth [141]. Utilizing a COF/NH_2-$Ti_3C_2T_x$ MXene heteroconjugate (COFs made of 1,3,5-triformylbenzene and p-phenylenediamine) as a Li host showed that the Li-N interactions can distribute Li ions inside all the COF channels uniformly leading to the Li nucleation (inhibition of the dendrite growth), a rapid ion accessible interface, and increased Li nucleation/deposition kinetics [106]. The rapid Li ions transport and even deposition on the MXene@COF resulted in improved Coulombic efficiency (CE) with stability over 300 cycles under high current densities of up to 20 mA cm^{-2} which was much higher than that for the individual MXenes, COFs, and bare Cu as hosts for Li ions. Importantly, COF@MXene exhibited the specific capacity of 780 mAh g^{-1} after 150 cycles (capacity retention ~ 68 %) which is double the capacity of the Li/Cu||S cell that stopped working after 110 cycles.

Covalently conjugated COF@MXene hybrids and the physically mixed COF@MXene composites can positively affect the Li anode. Comparison of the Li deposition at the current density of 0.2 mA·cm^{-2} for the pristine MXene film and the COF@MXene film (prepared by vacuum filtration of a mixed dispersion of MXenes and COFs made of *p*-phenylenediamine and 1,3,5-triformylbenzene) showed the formation of dendrites on the MXene film. However, a dense and uniform Li layer without dendrites was deposited on the COF@MXene film [142]. Notably, the nucleation overpotential of Li on the MXene film was 130.5 mV whereas the presence of the lithiophilic COFs in the COF@MXene film reduced it to 73.5 mV. Lower nucleation overpotential affords uniform and dendrite-free Li deposition [143]. The uniform and dense Li layer minimizes the consumption of the deposited Li by a side reaction which results in higher Coulombic efficiency for the COF@MXene (>97 %) than the MXene film (≈70 %) at 1 mA·cm^{-2}. Assembly of a Li-S battery with the Li/COF@MXene anode and a sulfur/polyacrylonitrile cathode displayed a specific capacity of 1192 mA h g^{-1} at 1 C with 73.8 % retention after 300 cycles. Coating Li foil anode surface with COF@NH_2-$Ti_3C_2T_x$ heteroconjugate and its application in lithium metal battery showed it could form Li dendrites and stabilize Li anode [144]. High flexibility, excellent mechanical properties, great lithiophilicity, and the presence of transport channels for Li^+ inside the MXene/COF layer provide a consistent Li^+ flux and controlled sites for the deposition of Li. Therefore, the Li dendrite growth and expansion of the electrode size is strongly inhibited. The corresponding Li||Li symmetrical cell exhibited stable performance for 5000 h and 600 h operation by working, respectively, at and 1 and 5 mA cm^{-2}/10 mAh cm^{-2}.

Another method to mitigate the shuttle effect in Li-S batteries is the modification of the polypropylene (PP) separator by coating it with various materials such as graphene oxide, carbon nanotube, and metal oxides [145–147]. Utilizing the positively charged COFs with high porosity can trap the negatively charged polysulfides via electrostatic interactions and suppress the shuttling effect. Accordingly, vacuum filtration of a COF@MXene (COF made of triaminoguanidine hydrochloride with 1,3,5-triformylphloroglucinol) on the surface of a commercial PP separator provides a suitable membrane to be used as a separator in Li-S batteries [107]. In addition to the positive effect of the COFs in improving polysulfide sequestration and Li-ion conduction, the high conductivity and catalytic activity of MXenes accelerate the conversion of the intercepted polysulfides. This synergistic property endows carbon nanotube/sulfur cathodes with good electrochemical performance, having negligible average capacity decay (0.006 %) per cycle within 2000 cycles at 2 C. Additionally, the corresponding Li-S battery showed a specific capacity of 1280 mA h g^{-1} at 0.1 C with retained capacity of 1186 mA h g^{-1} after 200 cycles.

Vanadium flow batteries (VFBs) are another group of energy storage systems with great importance due to their flexibility, high energy efficiency, long service life and high safety [148,149]. The proton exchange membrane (PEM) in VFBs has a critical role in the proton transfer process and preventing the vanadium ions transfer between the positive and negative electrodes [150,151]. The COF-based composite membranes have found application in VFBs due to the large surface area and adjustable pore size in COF structures [152,153]. However, the poor dispersibility of COFs within various solvents makes the uniform distribution of COFs within polymer matrices a big challenge. The conjugation of COF to MXene can provide the corresponding COF@MXene hybrid with better dispersibility in polymer matrices. Jia et al. showed that a composite membrane made of sulfonated polyether ether ketone (SPEEK) matrix containing COF@MXene filler (with COF synthesized from melamine and terephthalaldehyde) has a more uniform and homogenous structure compared to the one containing only COF as filler indicating better compatibility between SPEEK and COF@MXene than with pristine COF [154]. COF@MXene/SPEEK membrane showed nearly similar proton conductivity as SPEEK whereas the proton conductivity of COF/SPEEK membrane was very weak probably due to the agglomeration of COF within the membrane which blocks the membrane's pores. Notably, while the pore size in COF is smaller than the size of VO^{2+} ions, increasing the COF content increased the permeability of the COF/SPEEK membrane toward VO^{2+} due to the COF agglomeration. In contrary, increasing the COF@MXene content in the membrane continually reduced the VO^{2+} permeability due to the excellent dispersibility of COF@MXene within the SPEEK and no agglomeration. Practically, lower VO^{2+} permeability improved the coulombic efficiency (CE) and voltage efficiency (VE) of the corresponding VFB battery. The energy efficiency (EE) of the VFB with COF@MXene/SPEEK membrane at 40 mA cm^{-2} reached 93 % whereas the value with the SPEEK membrane was only 86 %.

Zinc-air batteries (ZABs) are next-generation batteries due to their copious zinc source and high theoretical capacity density [155]. The design and structure of air cathodes in ZABs are the main challenges and they usually require complex bifunctional catalysts. The slow oxygen-intermediate reaction reduces the specific capacity and output power without a proper cathode. The usual air cathodes are based on noble metals and their highly expensive oxides. Conductive Nb_2CT_x MXene has been used as an electrode for the oxygen evolution/reduction reaction (OER/ORR). However, agglomeration and self-accumulation of the flakes in Nb_2CT_x MXene can decrease the reaction kinetics. Additionally, using porous COFs in ZABs as electrocatalysis supports the adsorption/desorption of oxygen intermediates [156,157]. Combining COFs with Nb_2CT_x MXene can overcome the shortcomings of each component. Comparing the performance of Nb_2AlC MAX, Nb_2CT_x MXene, COF@Nb_2CT_x MXene (COF composed of *p*-phenylenediamine and 1,3,5-triformylbenzene), and IrO_2 as cathode electrodes revealed the overpotentials (E_{j10}) of 550, 435, 373, and 360 mV, respectively [158]. Additionally, the potential difference ($\Delta E = E_{j10} - E_{half}$) of COF@$Nb_2CT_x$ (ΔE = 0.79 V) was only a little higher than that of Pt/C and IrO_2 ($\Delta E = 0.77$ V) as the control electrode. This indicats the excellent performance of the COF@Nb_2CT_x MXene electrode. Coating the air electrode in ZAB with COF@Nb_2CT_x MXene leads to the continual occurrence of a half-reaction of OER and ORR (Fig. 16a,b). The power density of COF@Nb_2CT_x MXene as an air cathode was 75 mW cm^{-2} which is lower than the standard Pt/C + IrO_2 (105 mW cm^{-2}) cathode (Fig. 16c). However, the specific capacity of COF@Nb_2CT_x (545 mAh g^{-1}) was comparable to that of Pt/C + IrO_2 (550 mAh g^{-1}) (Fig. 16d). Notably, the charge-discharge cycle COF@Nb_2CT_x MXene-based ZAB remained stable after 120 h overcoming the low stability of noble-metal-based ZABs (Fig. 16e).

5.2.2. COF@MXene hybrids in Supercapacitors

Supercapacitors are energy storage devices with ultrafast charge-discharge ability and long cycling life. Developing new electrodes to obtain high-performance supercapacitors is critical. High stability, excellent and tunable porosity, diverse and pre-designable structures, and tunable redox potentials render COFs as capable electrodes in supercapacitors. One of the main challenges of COFs in supercapacitors is their poor specific capacitance and low electrical conductivity.

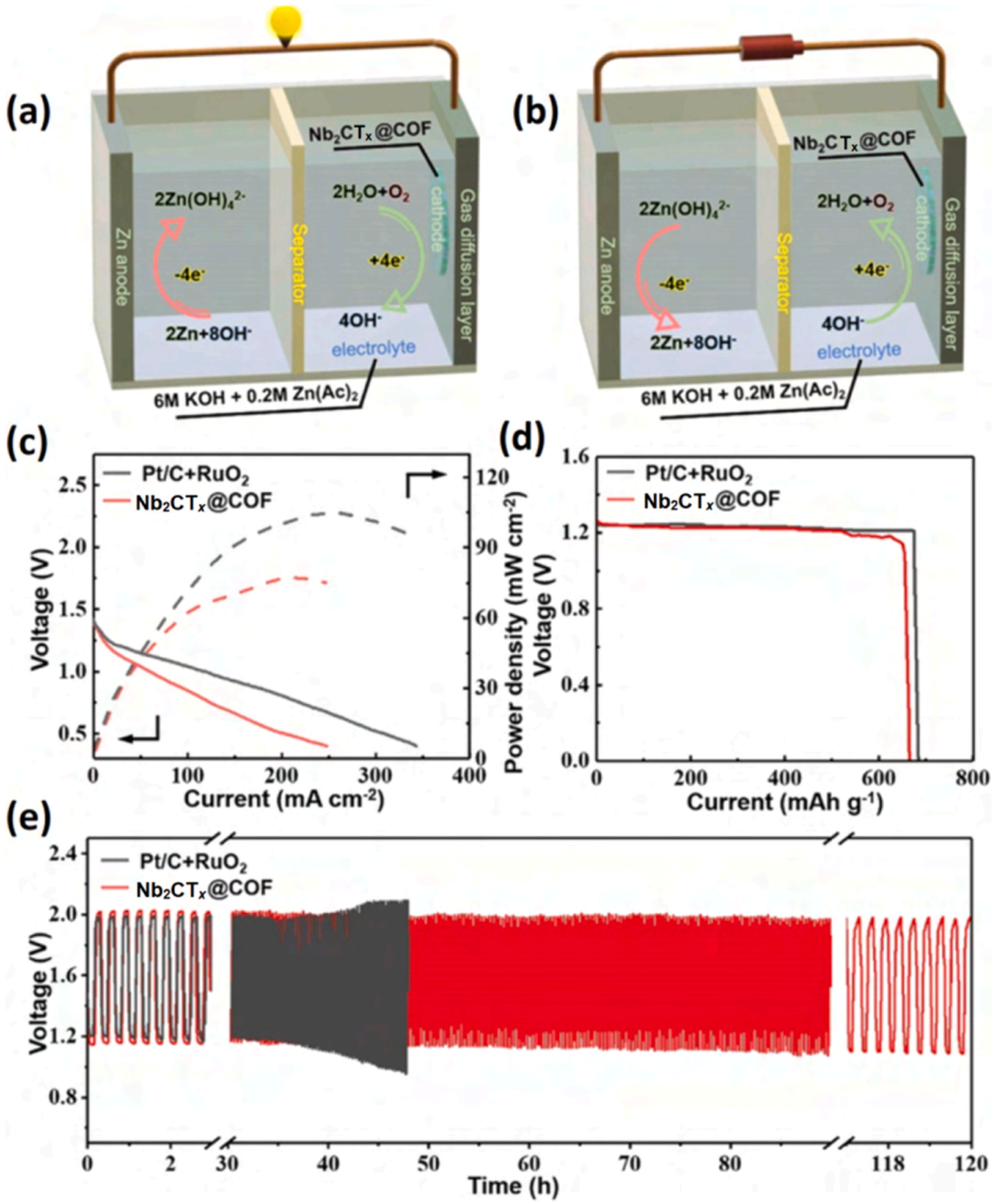

Fig. 16. (a,b) Description of the discharging and charging processes in ZAB batteries with COF@Nb_2CT_x MXene as an air cathode. Comparing the (c) polarization plots and power density, (d) discharging at 5 mA cm^{-2}, and (e) long-term charge-discharge cycling stability of the COF@Nb_2CT_x MXene cathode with the Pt/C + RuO_2 cathode [158]. Reproduced with permission from American Chemical Society, 2022.

Incorporating the redox-active groups (such as quinone groups) in the structure of COFs and their hybridization with conductive materials can significantly improve the performance of COFs in supercapacitors [159, 160].

On the other hand, MXenes with metal-like electrical conductivity, tunable surface chemistry, and excellent volumetric capacitance have found great potential in supercapacitors [161]. Therefore, combining the homogeneous pore channels of COFs (which can improve the electrolyte ions adsorption and transportation and thereby enhance the electrode rate capability) with the high conductivity of MXenes is a promising approach for fabricating high-performance supercapacitors. Accordingly, a COF/NH_2-$Ti_3C_2T_x$ MXene hetero-conjugate bearing a redox-active-containing COF (composed of 2,6-diaminoanthraquinone and 2,4,6-triformylphloroglucinol) was used as the working electrode for the assembly of a three-electrode supercapacitor system with Pt and Ag/AgCl, respectively, as the counter electrode and the reference electrode [162]. The cyclic voltammetry (CV) curves of the COF@MXene electrode showed a reversible redox peak at 0.75 V indicating its pseudocapacitive behavior. This reversible peak originated from the dynamic transformation between the quinone (C═O) and hydroquinone (C-OH) groups in 2,6-diaminoanthraquinone of the COFs. The slightly distorted triangle shape of the galvanostatic charge-discharge (GCD) curve of the COF@MXene electrode further confirmed its pseudocapacitive behavior. Notably, with a specific capacitance of 290 F g^{-1} at a current density of 0.5 A g^{-1} and 102.8 % capacitance retention after 1000 cycles, this COF@MXene showed excellent performance as an electrode for supercapacitor in a Na_2SO_4 electrolyte. Utilizing a free-standing COF@MXene film electrode fabricated through vacuum filtration of a mixed dispersion of redox-active COF (composed of 2, 6-diaminoanthraquinone and 2,4,6-triformylphloroglucinol) with $Ti_3C_2T_x$ MXene nanosheets, in a three-electrode supercapacitor system afford a specific capacitance of 390 F g^{-1} at 0.5 A/g, which was 12 times higher than that of the pristine COFs [163]. An all-solid-state supercapacitor based on this COF@MXene electrode showed an energy density of 27.5 Wh kg^{-1} at a power density of 350 W kg^{-1}, a maximum power density of 7000 W kg^{-1} at an energy density of 19.7 Wh kg^{-1}, specific capacitance 390 F g^{-1} at 0.5 A/g and an excellent capacitance retention of 88.9 % after a 20000 charge/discharge cycling.

Assembly of $Ti_3C_2T_x$ MXene on the surface of polydopamine-modified nylon 6 membrane followed by aminosilanization and *in situ* growth of COFs (made of hexaketocyclohexane octahydrate and 1,2,4,5-benzenetetramine tetrahydrochloride) produces a hierarchical-structured electrode for flexible supercapacitors [164]. The electrochemical performance of this COF@$Ti_3C_2T_x$/nylon as a working electrode in a three-electrode system with a 1 M H_2SO_4 electrolyte demonstrated a larger cyclic voltammetry (CV) curve than the $Ti_3C_2T_x$/nylon and the physically self-assembled COF@$Ti_3C_2T_x$/nylon which indicated its higher charge storage ability (Fig. 17a). Additionally, the galvanostatic charge-discharge (GCD) (Fig. 17b) curve for the covalently assembled COF@$Ti_3C_2T_x$/nylon electrode showed a longer symmetrical triangular discharge time with a negligible voltage drop than the other two electrodes that indicats its high dynamic reversibility and high capacitance. The specific capacitance for the covalently assembled COF@$Ti_3C_2T_x$/nylon, physically assembled COF@$Ti_3C_2T_x$/nylon, and $Ti_3C_2T_x$/nylon electrodes were 1298, 830, and 548 F cm^{-3}, respectively (Fig. 17c). The covalently assembled COF@$Ti_3C_2T_x$/nylon and physically assembled COF@$Ti_3C_2T_x$/nylon electrodes, respectively, exhibited capacitance retention of 82.6 % (after 20000 cycles) and 68.4 % (after 10000 cycles). This results confnirm the critical role of the covalent conjugation between the COF and $Ti_3C_2T_x$.

The microfluidic technique was employed to assemble a vertically aligned $Ti_3C_2T_x$ MXene (VA-$Ti_3C_2T_x$) on a COF (made of 1,3,5-triformylbenzene and *p*-phenylenediamine) for the fabrication of hybrid fibers for use in high-performance electrochemical supercapacitors [165]. The molecular dynamics (MD) simulation showed that the diffusion of H^+ through conventional MXene-based electrodes is minimal due to the tortuous pathways. In contrast, in microfluidic-made electrodes, the pathway is vertical and shortened, improving the electrochemical reaction kinetics (Fig. 17d,e). The most considerable CV (Fig. 17f) was achieved for the COF@VA-$Ti_3C_2T_x$ MXene electrode containing 30 wt%

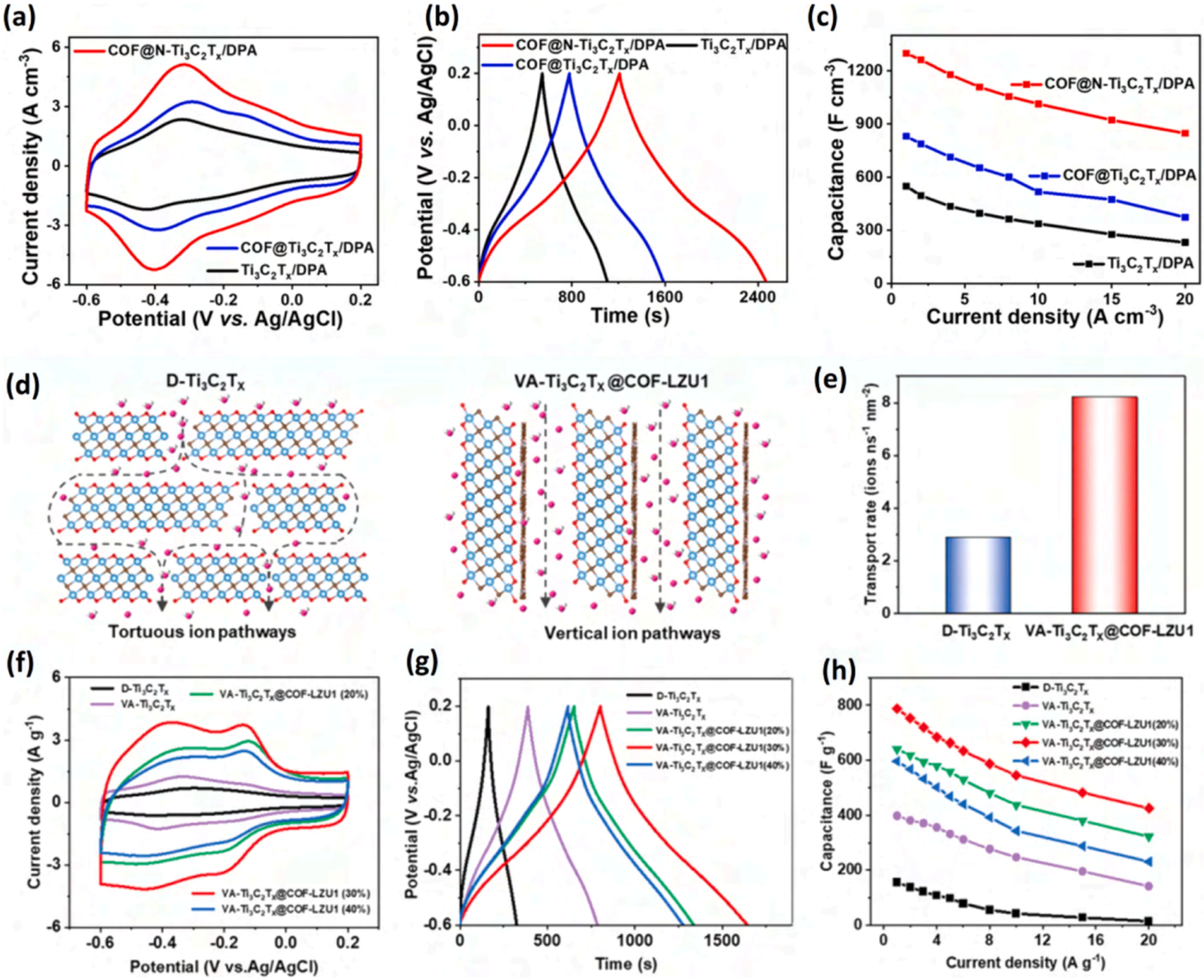

Fig. 17. Electrochemical evaluation of different electrodes in a 1 M H_2SO_4 electrolyte through a study of (a) cyclic voltammetry curves at 2 mV s^{-1}, (b) galvanostatic charge-discharge curves at 1 A cm^{-3}, and (c) specific capacitances at different current densities[164]. (d) The ion transport pathways for the disordered MXene (D-$Ti_3C_2T_x$) and COF@VA-$Ti_3C_2T_x$. (e) The transport rate of proton (H^+) in D-$Ti_3C_2T_x$ and COF@VA-$Ti_3C_2T_x$. Electrochemical evaluation of different electrodes in 1 M H_2SO_4 electrolyte through the study of (f) cyclic voltammetry curves at 2 mV s^{-1}, (g) galvanostatic charge-discharge curves at 1 A cm^{-3}, and (h) specific capacitances at different current densities[165].

(a) Reproduced with Permission from Wiley, 2023. (b) Reproduced with Permission from Wiley, 2023.

COF through the study of the electrochemical properties of different MXene-based electrodes in a three-electrode system in a 1 M H_2SO_4 aqueous electrolyte which indicated its higher charge storage ability. Also, the galvanostatic charge-discharge (GCD) (Fig. 17g) curve for the COFs (30 %) @VA-$Ti_3C_2T_x$ MXene electrode demonstrated a longer symmetrical triangular discharge time with a slight voltage drop compared with other electrodes, confirming its higher dynamic reversibility and higher capacitance. The COF (30 %)@VA-$Ti_3C_2T_x$ MXene electrode showed a specific capacitance of 787 F g^{-1} at 1 A g^{-1} (Fig. 17h). All-solid-state fiber-shaped asymmetric supercapacitors (FASCs) based on this electrode demonstrated a high energy density of 27 Wh kg^{-1} with an 89 % capacitance retention after 20000 cycles.

5.3. Hybrid Membranes for Water Treatment and Purification

Combining porous COFs with 2D MXenes creates hybrid materials suitable for separation and purification applications. These materials can be utilized for different purification methods, such as the adsorption of pollutants, the development of separation membranes, and electrochemical deionization. Table S6 presents a list of the COF@MXene hybrids employed in various water purification processes.

2D nanomaterials have found great potential in fabricating ultrathin membranes with narrow interlayer nanochannels in separation processes. The uniform distribution of diverse functional groups on the MXenes surface renders their nanosheets homogeneous and well-aligned nanochannels [166]. Practically, MXenes create slit-like 2D nanochannels as a result of the available spacing between the nanosheets (interlayer spacing). Typically, the interlayer spacing in MXene membranes is about 3.5 Å and 6 Å, in their dry and wet states, respectively. The smaller size of these nanochannels than the size of bacteria, pharmaceuticals, hormones, dyes, and nanoparticles enables the efficient removal of these impurities from the water stream [167,168]. Despite these advantages, susceptibility to oxidation in water [169], tendency to restack, and swelling in water [166,170] restrict the full utilization of MXene-based membranes in water treatment and purification. It was shown that the oxidation of delaminated MXene membranes results in the appearance of holes in the membrane [171]. These holes increase the size of the membrane channels which in turn lead to the water flux enhancement. The oxidation reactions mainly happen at defect sites and the edges. Furthermore, it is important to note that the oxidation of MXene nanosheets is size-dependent and smaller flakes have lower resistance to oxidation. Therefore, the use of larger nanosheets for the fabrication of MXene membranes is preferred [172]. In another strategy, the incorporation of ascorbic acid, as antioxidant, and aluminum ions, to prevent swelling of the $Ti_3C_2T_x$ layers by their crosslinking, led to the fabrication of a membrane with no performance decline within 30 days [173]. Also, covering the defect points with cations can prevent or delay oxidation without changing the structure of MXene or attaching any molecules that can be useful in applications in water membranes. However, the addition of cations can alter the surface charges of 2D sheets and could affect the stacking of the flakes which requires further studies to best design a membrane with desired channel sizes [174]. Even in stabilized MXene-based membranes, the presence of long and tortuous nanochannels delays the mass transfer and reduces the water permeation through the pristine MXene membranes [175,176]. Pathways with larger diameters and shorter lengths provide faster permeation. Incorporating intercalators in the MXene membranes can enlarge the interlayer nanochannels [177]. The fabrication of ultrathin membranes with less tortuous pathways is an effective strategy for reducing the length of the transport. 2D COFs are suitable candidates for this application by providing short and straightforward pathways. Coating MXene nanosheets with a COF layer can change the nanosheets interlayer spacing. For example, the N_2 sorption isotherm revealed the pore size distribution of 0.8–10 nm for a MXene/COF hybrid membrane whereas the interlayer spacing of neat MXene membrane was around 1.34 nm [178]. Moreover, Wang et al. reported that the covalent conjugation of superhydrophobic COF to the MXene surface significantly improve the oxidation resistance of membranes and prevents the swelling of these membranes in water during the water treatment process [179]. As a result, if COF can uniformly cover the whole MXene surface, it may address the restacking and oxidation stability issues of MXenes [180]. The COF layers prevent the restacking and oxidation of MXene nanosheets and therefore maintain the membrane performance during the desalination and regeneration process.

The combination of COFs and MXenes can improve the flux, adsorption capacity, and selectivity of the hybrid composites in water treatment applications [178,181]. Accordingly, a bilayer COF-MXene membrane was prepared by the sequential vacuum filtration of a COF (made of *p*-phenylenediamine and 1,3,5-triformylphloroglucinol) and $Ti_3C_2T_x$ MXene dispersions on a macroporous nylon substrate [181]. The synergistic effect of the COF and MXene on the membrane structure is schematically depicted in Fig. 18a-b. SEM images showed a macroporous structure for the bare nylon substrate, whereas after coating by a COF layer with a thickness of 102 nm on the substrate (Fig. 18c-e), a smoother porous surface with an average pore diameter of 16 nm was prepared. A bilayer membrane with a dense and wrinkled surface morphology was fabricated by subsequent coating with the $Ti_3C_2T_x$ layers with a tunable thickness of 8–19 nm (Fig. 18f-h). Under the optimum condition, the dual-layer membrane provided high permeance of 563 L m^{-2} h^{-1} bar^{-1} and high rejection of 99.6 % against Congo Red. The high thickness of the MXene layer results in long and tortuous pathways leading to high rejection.

On the other hand, the porous COF layer provides shorter pathways and faster permeations, but their large crispation-induced pores cannot prevent the transport of solutes. Therefore, a combined optimized COF@MXene membrane can provide both high flux and rejection [182]. Vacuum filtration of COF@$Ti_3C_2T_x$ MXene (COF composed of 1,3,5-triformylbenzene and *p*-phenylenediamine) on the surface of PVDF membrane affords a superhydrophobic membrane for oil-water separation [179]. This membrane with a water contact angle of 156° and an oil contact angle of 0° exhibited ultrahigh permeation fluxes of 54280 L m^{-2} h^{-1} and 643200 L m^{-2} h^{-1} bar^{-1} for a water-chloroform emulsion, respectively, for gravity-driven and external pressure-driven processes. Notably, after 10 cycles, the separation efficiency of the membrane maintained above 99 %, with a negligible drop in flux. In addition, washing the membrane with ethanol after each set of 10 cycles resulted in nearly full recovery of the membrane performance. The sequential vacuum filtration of a hydrophilic COF-SO_3H (made of 1,3,5-triformylphloroglucinol and 2,5-diaminobenzenesulfonic acid) and MXene on a NaOH-treated microporous nylon filter membrane, results in a COF@MXene membrane with adjustable water permeance and dye rejection [183]. Enhancing the density of the COF layer improved the rejection rates and reduced the permeance. Under optimal conditions, a COF layer density of 37 μg cm^{-2} exhibited a rejection rate of 80.3 % for Congo red dye with a water permeance of 626.2 L m^{-2} h^{-1} bar^{-1} . By casting a layer of MXene on the surface of COF at a MXene:COF ratio of 0.5 wt%, the rejection increased to 96.7 %, and water permeance reduced to 356.6 L m^{-2} h^{-1} bar^{-1} .

Yang et al. developed covalently assembled COF@NH_2-$Ti_3C_2T_x$ MXene heteroconjugate adsorbents (COF made of 1,3,5-tris(4-aminophenyl)benzene (TAPB) and 4,4,4-(1,3,5-triazine-2,4,6- triyl)tribenzaldehyde (TTB)) for removal of antibiotic pollutions (fluoroquinolones) from aqueous media [184]. The maximum adsorption capacities of the pristine COFs and MXenes for different fluoroquinolones were in the range of 16–64 and 27–34 mg·g^{-1}, respectively, which increased to 54–148 mg·g^{-1} for the COF@MXene heteroconjugate. Notably, the adsorbent showed a protein exclusion efficiency of > 97 %. The adsorbent could be regenerated by washing with 0.1 M HCl. After six adsorption/desorption cycles, the adsorption efficiency of COF@MXene slightly reduced to 79 %.

Capacitive deionization (CDI) is a water deionization electrochemistry technique. Porous carbons with acceptable conductivity have been

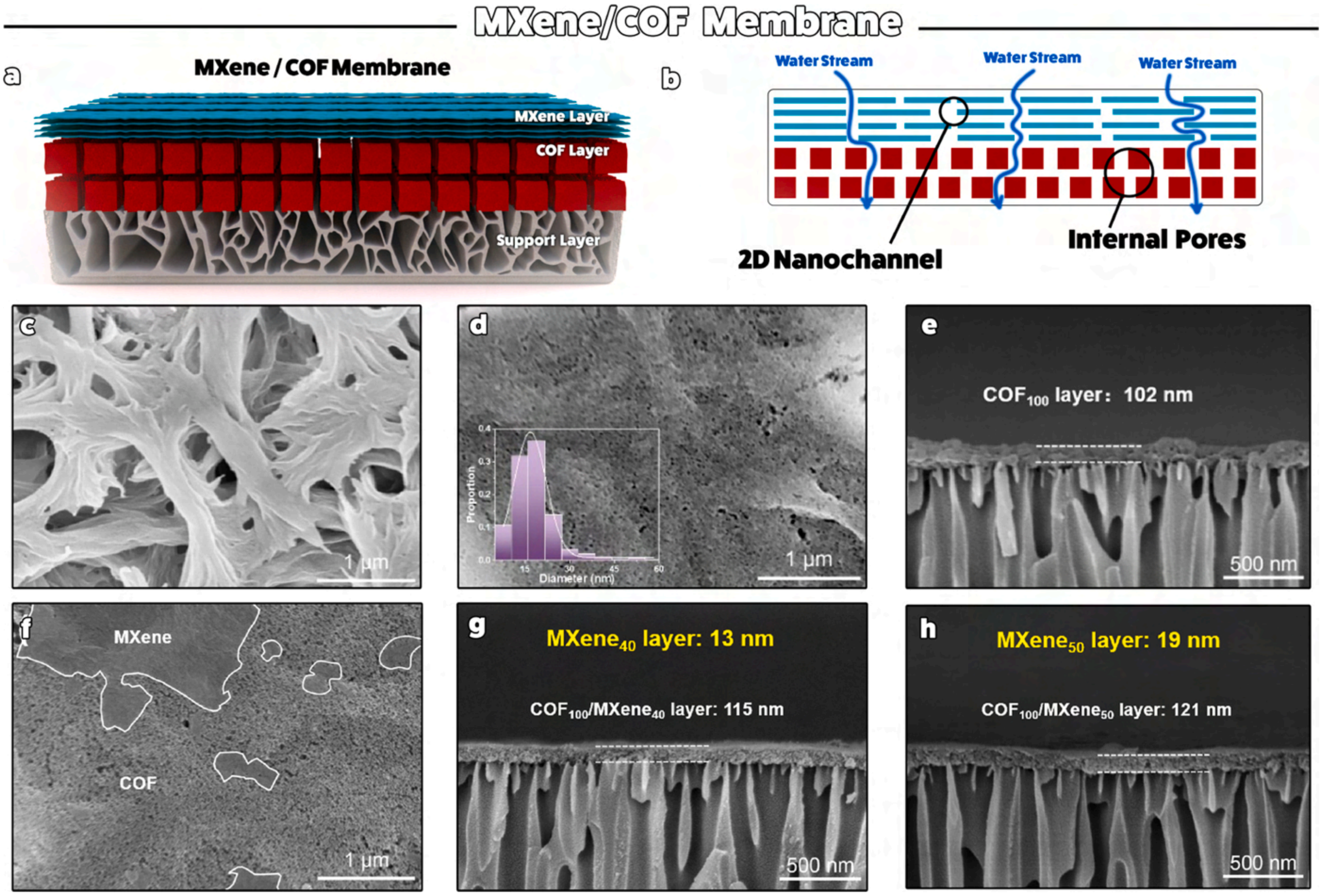

Fig. 18. Schematic description of (a) and (b) water permeation mechanisms using a hybrid COF@MXene membrane, SEM images of the (c) top surface of the nylon substrate, (d) top surface of the COF/nylon membrane, and (e) cross-section of the COF/nylon membrane. SEM images of the (f) top surface and (g,h) cross-section of the MXene/COF/nylon membranes with different MXene loadings (The low MXene content, thickness 8 nm, cannot fully cover the surface of the COF layer). [181]. Reproduced with Permission from Elsevier, 2022.

used as typical electrodes for CDI [185,186]. However, porous carbons usually possess low salt adsorption capacity (SAC) and weak cycling stability in natural oxygenated saline water, limiting their broad applications [187]. MXenes are potentially good alternatives for the porous carbons in the CDI process due to their high electrochemical capacity, excellent conductivity, reversible ion intercalation/deintercalation, and high hydrophilicity. However, aggregation, restacking, and oxidation of MXenes restrict their long-term utilization for this application. These issues can be overcome by coating a layer of COFs on the surface of MXenes. While MXenes provide high electrical conductivity, the coated COFs layer protects the MXene layers from oxidation during the desalination/regeneration process. Accordingly, a core-shell COF@NH_2--$Ti_3C_2T_x$ MXene architecture (COF composed of 2, 6-diaminoanthraquinone (DAAQ) and 2,4,6-triformylphloroglucinol (TFP)) was developed in which the COF nanorods were uniformly grown on the surface of MXene nanosheets [188]. While MXenes showed a relatively low specific surface area (155 m^2 g^{-1}), the COF@MXene showed a high specific surface area of 424 m^2 g^{-1}. High surface area, excellent conductivity, and abundant redox-active quinone groups render the obtained COF@MXene superior electrochemical properties for utilization in CDI. The cyclic voltammetry (CV) in a NaCl electrolyte showed the reversible redox peaks related to the quinone/hydrnoquinone redox process of DAAQ of the COF segment. Therefore, the COF@MXene-based electrode can reversibly capture/release Na^+ in the CDI process. The CDI desalination process over oxygenated saline water using MXene@COF electrode showed a NaCl adsorption capacity of 53.1 mg g^{-1} with a stable cycling performance over 100 CDI cycles.

5.4. Biosensors and Electrochemical Platforms Using COF@MXene

The low cost, easy use, high sensitivity, and portability of electrochemical-based biosensing endow it with a wide application in clinical diagnosis, food analysis, and environmental monitoring [189]. MXenes [112] and COF [113] have been used to develop biosensors. Synergistic effects of COFs and MXenes can provide composites with improved sensitivity in analysis. Table S7 provides a list of COF@MXene hybrids applied in analyzing different analytes using various analytical techniques.

Accordingly, a peptide(Pep)-target-aptamer(Apt) biosensor for the Norovirus (NoV) detection was prepared by modification of a glassy carbon electrode (GCE) with Pep@Au@BP@$Ti_3C_2T_x$ MXene and utilizing magnetic Apt@Au@$ZnFe_2O_4$@COF nanocomposite as the probe material (Fig. 19) [190]. Specific binding between Pep or Apt with NoV renders the formation of a sandwich biosensor in the presence of NoV. The content of NoV was determined indirectly by incorporating toluidine blue (TB) as a redox probe at Au@$ZnFe_2O_4$@COF. A higher TB signal was directly related to the higher NoV content. This biosensor could detect the NoV in the 0.01–105 copies/mL range, with a detection limit (LOD) of 0.003 copies/mL.

Assessing the reproducibility and repeatability of this biosensor by measuring the peak current of five electrodes in detecting 10^4 copies/mL NoV showed a similar current response for all five electrodes indicating a good reproducibility. Furthermore, the stability of the biosensor was analyzed by assessing its performance after being stored at 4 °C for 14 days. The current response of the sensor remained > 95.5 % of the initial

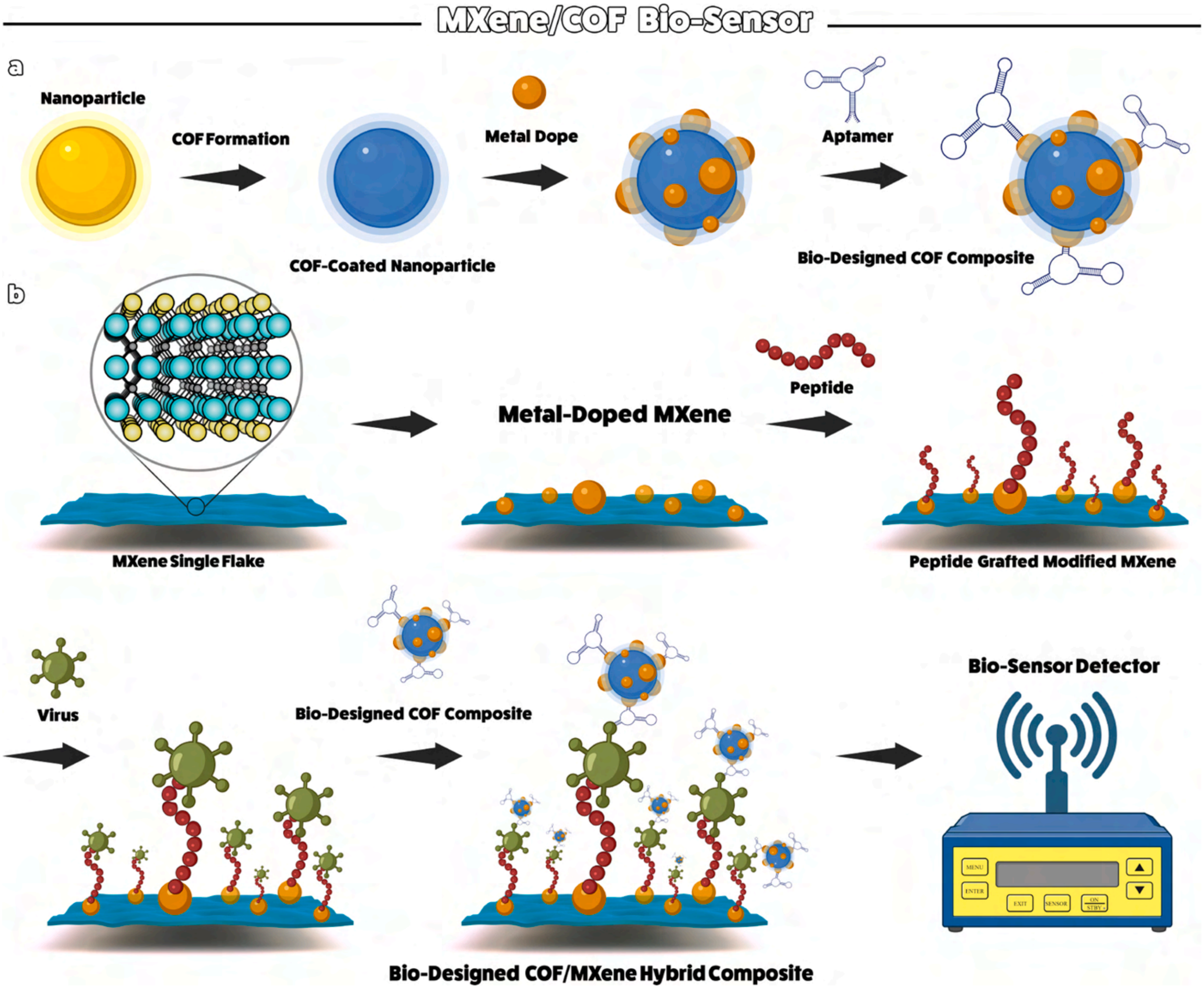

Fig. 19. (a) Preparation of Apt@Au@$ZnFe_2O_4$@COF, and (b) assembly of the NoV electrochemical biosensor with MXenes [194]. Reproduced with Permission from Elsevier.

value, indicating good stability. Importantly, it could detect the NoV in real fluid analytes. Indeed, the results of the detection of NoV in stool samples using the COF@MXene biosensor was 100 % comparable to the results obtained from the reverse transcription quantitative polymerase chain reaction (RT-qPCR) technique. This indicates that the COF@MXene biosensor's response in real samples is highly reliable.

Detection of low concentrations of biomarkers in biological fluids is critical for early diagnosis of various diseases such as cancers and Alzheimer's. The amyloid-beta oligomers (Aβ1–42) have been reported as biomarkers for Alzheimer's [191]. Therefore, detecting low concentrations of these biomarkers is important in providing quick treatment to inhibit the progress of diseases. Accordingly, LV et al. reported the fabrication of an electrochemical biosensor for the detection of Aβ1–42 oligomers in human serum by the combination of aptamer-gold-modified MXene (Apt@Au-$Ti_3C_2T_x$ MXene) as the glassy carbon electrode modifier and Apt/TB-Au@COFs (TB: toluidine blue) as the probe [192]. Due to the dual amplification strategy and strong affinity of aptamer toward the biomarker, the Aβ1–42 oligomers could be captured and detected with high sensitivity and selectivity by both Apt/TB-Au@COFs labels and Apt-modified Au@MXene substrate. Under optimum conditions, this platform could detect Aβ1–42 oligomers in a wide linear range of 0.01–180 pg mL^{-1} with a low limit of detection (LOD) of 4.27 fg mL^{-1}. The current response of the biosensor was reduced by 6.17 % from the initial detection value after being stored for 40 days at 4 °C, indicating the fair long-term stability of the biosensor performance. Notably, the comparative evaluation for detecting Aβ1–42 oligomers in the serum of human samples by this sensor showed almost the same result as a standard enzyme-linked immunosorbent assay (ELISA) kit, indicating the reliability of the sensor's response for practical applications. A similar electrochemical immunosensor for the detection of CYFRA21–1, as a key biomarker of lung cancer, was reported through the combination of antibody@gold-modified MXene (Ab@Au-$Ti_3C_2T_x$) as the sensor substrate signal enhancer and antibody/toluidine blue modified AuNPs-doped COF (Ab@TB-Au-COF) as the probe [193]. This sensor could detect the CYFRA21–1 biomarker at 0.5–1.0 × 10^4 pg mL^{-1} with a detection limit of 0.1 pg mL^{-1}.

The measurement of the response of five individual electrodes using square wave voltammetry (SWV) showed similar current responses with a relative standard deviation (RSD) of 3.6 %, indicating the good reproducibility and accuracy of this sensor. Additionally, the current response of these electrodes decreased to 85.5 % of the initial response after storing the electrodes at 4 °C for 18 days which indicate a mild stability of the sensor over time. Notably, adding a specific amount of CYFRA 21–1 to normal human serum (NHS) and then measuring by

COF@MXene sensor showed that the accuracy of the measurement was in the range of 93.2–96.6 %. This indicates the excellent selectivity of the sensor towards CYFRA 21–1 so that the presence of interfering components in the real human serum does not influence the response of the sensor. Also, dilution the human serum medium 100 times and mixing with different concentration of CYFRA 21–1 and then evaluating by the sensor showed a recovery rate of 98.6–102.6 % with an RSD of < 3.8 % indicating the ability of the sensor in detection low concentration of CYFRA 21–1 in real biological samples.

Coating the surface of glassy carbon electrode (GCE) with a COF@MXene hybrid (COF composed of 2, 4, 6-triformylphloroglucinol and *p*-phenylenediamine) provide a suitable substrate for the deposition of Au nanoparticles and fabrication of COF@MXene/Au electrode [195]. Further conjugation of thiolated-β-CD to the Au surface provides a supramolecular recognition system for selective detection of zearalenone via the host-guest interaction approach. A working electrode based on COF@MXene/Au/βCD composite could detect zearalenone with a linear response range of 0.04–0.5 µg/mL and a detection limit of 0.01 µg/mL. Furthermore, adding a specific amount of zearalenone to blank wheat and barley and then measuring with this sensor showed a recovery rate of 96.6–108.9 % which was comparable with the results obtained from UHPLC-MS/MS as the standard method.

One method for determining very low concentrations of analytes is the solid phase microextraction (SPME) strategy, in which, the enrichment of the target analyte is achieved by an adsorbent in the first step [196]. The structure of SPME fibers strongly affects the performance of the system. The porous structure of COFs with a high specific area and diverse types of functional groups renders them good adsorbent materials for SPME processes [197]. Therefore, combining COF adsorbents with conductive MXenes is a promising approach for the fabrication of more efficient SPME systems. Accordingly, the surface of stainless steel wires was coated with COF@NH_2-$Ti_3C_2T_x$ MXene heteroconjugate (the COF was made of 2,5-dihydroxyterephthalaldehyde and 1,3,5-tris (4-aminophenyl)benzene) for developing an SPME fiber for detecting polycyclic aromatic hydrocarbons (PAHs) in honey samples [198]. By coupling this SPME system with gas chromatography, different types of polycyclic aromatic hydrocarbons in honey samples could be detected in a linear range of 2.0–2000 ng g^{-1} with a limit of detection (LOD) of 0.20–0.60 ng g^{-1}. The recovery of polycyclic aromatic hydrocarbons was in the range of 73–112 %. Notably, the COF@MXene fiber could be regenerated through desorption by heating at 280 °C for 7 min. The recycling of this fiber for over 300 extraction/desorption cycles showed no decline in its performance indicating its notable chemical and mechanical stability. Furthermore, adding different concentrations of PAHs in the level of ng/g to four different types of honey and then evaluating the recovery rate using SPME fiber showed the recovery rates of 73.2–112 % with a RSD of 3.5–8.7 % indicating an acceptable level of accuracy for this fiber.

Similarly, coating of a silanol-functionalized stainless steel substrate with COF@NH_2- $Ti_3C_2T_x$ MXene heteroconjugate (the COF was composed of 1,3,5-triformylphloroglucinol (TFP) and 4,4',4''-(1,3,5-triazine-2,4,6-triyl)trianiline) affords SPME fibers for detection of organochlorine pesticides (OCPs) traces [199]. The measured BET surface area and the pore volume for the pristine MXenes were 147 m^2 g^{-1} and 0.66 cm^3 g^{-1}, respectively; these values increased to 442 m^2 g^{-1} and 1.12 cm^3 g^{-1} for the COF@MXene composite, demonstrating its excellent porosity. Notably, the pore size of COF@MXene was around 9.8 nm, which indicates its suitability for capturing the OCP molecules (size 0.68–1.04 nm). The corresponding COF@MXene-based SPME system showed a limit of detection (LOD) of 0.036–0.126 ng g^{-1} with a wide linear range of 0.12–20.0 ng g^{-1} with a slight decrease in performance after 100 cycling times. The addition of various concentrations of different OCPs into radish, tomato, apple, and peach samples, followed by measurement using this COF@MXene SPME fiber, showed the recovery rates of 92.0–104.2 % with RSDs values 4.1–11.2 %. This result indicates the acceptable performance of this fiber in the detection COPS in fruits and vegetables. Coating the surface of stainless-steel SPME blades with COF-SO_3H@NH_2-$Ti_3C_2T_x$ heteroconjugate provides another suitable SPME fiber for the extraction of monoamine neurotransmitters [200]. With a specific area of 41.5 m^2 g^{-1} and a pore size distribution in the range of 2–59.5 nm, this fiber demonstrates a mesoporous structure. By combining this SPME fiber with HPLC, under optimum condition, it could detect norepinephrine (NE) and epinephrine (EP) with a linear range 0.1–100.0 ng mL^{-1} and detect dopamine (DA) and serotonin (5-HT) with a linear range 1.0–300.0 ng mL^{-1} and LOD 0.015–0.030 ng mL^{-1}. Addition of determined content of monoamine neurotransmitters into rat serum samples and then measurement using this SPME-HPLC method revealed recovery rates of 90.3–118.3 % with RSDs values of 1.6–10.8 %. This implies the satisfactory accuracy of the developed SPME for the extraction and measurement of monoamine neurotransmitters from real samples.

Although the obtained results from the developed COF@MXene biosensors for selective detection of targeted analytes have exhibited satisfactory accuracy and reproducibility level, the complicated and multistep fabrication methods for developing of these sensors is a great challenge for translating their applications from the laboratory level to the clinical and real-world level.

5.5. Protective Coatings: Enhancing Corrosion Resistance with COF@MXene

MXenes research has gained attention in the anti-corrosion coating field in recent years [201]. Adding MXenes to common organic coatings can improve the anti-corrosion performance of the coating [202]. Addition of MXene as a filler in composite coatings can increase the diffusion paths for corrosive species which in turn can delay the corrosion process [203]. Additionally, MXene can increase the density of the coating and therefore improve the interface adhesion between the coating and metal. However, MXenes highly hydrophilic nature, low surface area, gradual accumulation, and oxidation weaken their full potential for anti-corrosion coating applications.

Pre-modification of MXene can be used to address its oxidation issues as filler in anticorrosion coatings. Ding et al. showed that doping MXene with carbon dots (CD) can improve its oxidation resistance in epoxy coatings [204]. The formation of Ti–O–C covalent bonds between MXene and carbon dots could inhibit the oxidation of $Ti_3C_2T_x$ nanosheets. In another approach, Ning et al. showed that grafting of 1-allyl-3-methylimidazolium bromide ($[BMM]^+Br^-$) to the MXene surface could improve the oxidation resistance of $Ti_3C_2T_x$ MXenes [205]. The in situ modification of MXene nanosheets by integrating MgAl-intercalated layered double hydroxide (LDH) layer increased the dispersibility of MXene nanosheets inside the epoxy resin and prevented the restacking and agglomeration of these nanosheets within the coating [206]. The anticorrosion and antiwear features of the epoxy resin coating containing MXene–MgAl–LDH were significantly stronger than those of the coating containing only MXene. It is important to note that even gradual oxidation of MXene and formation of TiO_2 can still improve the anticorrosion performance of the coating during. Indeed, the generated TiO2 nanoparticles can fill the voids in the coating and act as a kind of coating healing agent [207].

Coating MXenes with a layer of a COF is an alternative strategy to address these issues. Importantly, the porous structure of COFs endows the ability of loading with corrosion inhibitors and self-healing agents. Accordingly, Najmi et al. prepared a COF@MXene heteroconjugate (SMXC) by the *in situ* solvothermal growth of COFs (made of melamine and terephthalaldehyde) on the surface of NH_2-$Ti_3C_2T_x$ MXene and then loaded this composite with glutamate and zinc (II) (SMXCGZ) as organic and inorganic corrosion inhibitors, respectively [208]. The N_2 adsorption-desorption showed that the surface area of MXene (27.6 m^2 g^{-1}) was increased to 128 m^2 g^{-1} after coating with COFs, indicating an excellent host for loading corrosion inhibitors. Fabrication of nanocomposite coatings by adding the COF@MXene to the epoxy resin coating improved the anti-corrosion performance of the coating by around 200 %.

The SMXCGZ NP improved both barrier and active corrosion protection. Zinc-glutamate complexes were formed inside the COF pores (Fig. 20). The pH changes during electrochemical reactions trigger the release of these complexes to the metal surface which can retard the corrosion significantly. Utilizing these hybrid nanoparticles as corrosion inhibitors in aqueous media could reduce the corrosion rate of steel by 88 % and reduce the i_{corr} from 0.022 to 0.002 mm/year. Zinc-glutamate complexes are converted to more stable species. $Fe(Glu)_2$ and $Fe(Glu)_3$ are from glutamate, and Zn^{2+} reacts with OH^- generated from oxidation reactions to form $Zn(OH)_2$ (Fig. 20). In addition to the blockage role of SMXCGZ NPs for electrolyte diffusion, the release of zinc and glutamate can participate in corrosion reactions at the metal interface. The 2D structure of MXenes extended the diffusion pathway to the metal surface. The covalently grafted COFs improved the MXenes dispersion which could successfuly fill the pores in an epoxy matrix. Additionally, Fe-glutamate complexes and $Zn(OH)_2$ formation decrease the local pH and the possibility of coating delamination.

6. Conclusion

Combining COFs with MXenes has produced a new group of nanocomposite materials with improved performance and excellent synergistic effects. MXenes provide metallic conductivity and excellent photothermal and electrochemical properties, while the high porosity and tunable chemical configuration of COFs render the composite high stability and selective permeability to specific compounds. Covalent conjugation and physical mixing of MXenes with COFs are two main strategies for fabricating COF@MXene composites. For the covalent conjugation, COFs can be *in situ* produced and grafted on the MXene surface. Additionally, pre-treatment of MXenes with similar functional groups of COFs (for instance, fabrication of NH_2-MXene) is essential to guarantee the covalent conjugation between MXenes and COFs. Physically mixed COF@MXene composites can be prepared by directly mixing pre-fabricated COFs with MXenes or via *in situ* synthesis of COFs in the presence of MXenes. The main driving force in these cases is the electrostatic interaction between the negatively charged MXenes and the positively charged COFs. These composites can be used also for modifying the surface of membranes, electrodes, and other substrates for diverse applications.

The application of COF@MXene composites in different fields (such

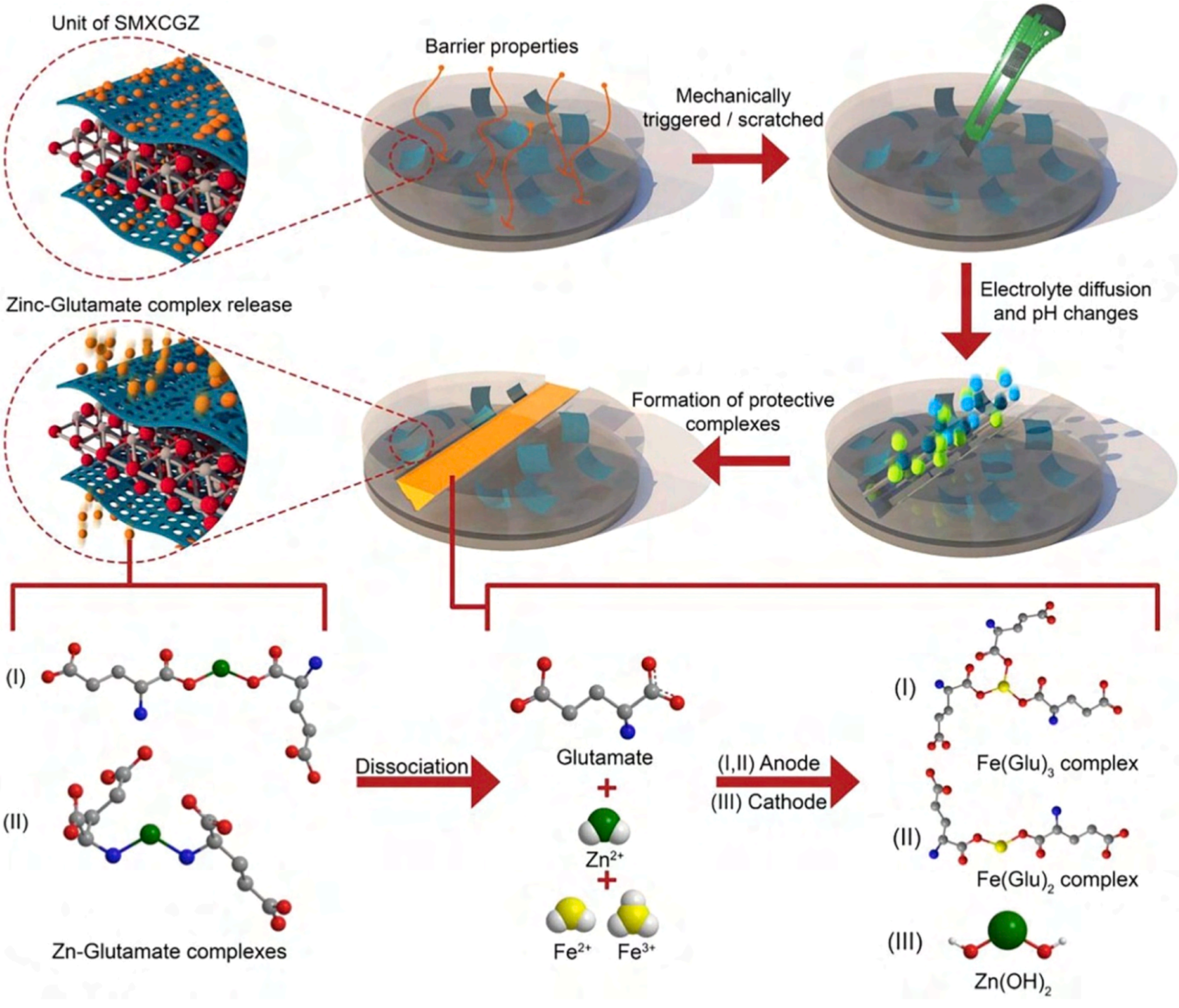

Fig. 20. Schematic illustration of active and barrier protection of SMXCGZ nanocomposite [208]. Reproduced with Permission from Elsevier.

as catalysis, energy storage, separation, sensing systems, and anti-corrosion coatings) has shown stronger performance than individual COFs and MXenes. For instance, in photocatalysis, narrow band gaps (close to zero) of MXenes significantly improve the electron-hole separation of COF@MXene composites and reduce the charge recombination rate. This feature renders stronger photocatalytic activity to COF@MXene composites compared to pristine COFs. In Li-S batteries, the high number of lithiophilic N sites in COFs and sulfurophilic Ti sites in $Ti_3C_2T_x$ MXene generate strong dual-site chemical interactions between the host and polysulfides. These synergistic effects can strongly suppress the shuttle effect and increase the lifetime of the batteries. The metal-like electrical conductivity of MXenes with high porosity of COFs can produce excellent electrodes for the fabrication of high-performance supercapacitors with ultrafast charge-discharge ability and long cycling life. While the thick MXene-based membranes exhibit low water flux in water purification due to their long, tortuous pathways, thinner membranes can be fabricated from COF@MXene composites with shorter pathways , higher fluxes, and excellent rejection rates.

7. Role of Computational Modeling in COF@MXene Hybrid Design

Theoretical methods, such as density functional theory (DFT), are critical in the design and optimization of advanced hybrid materials. In COF@MXene composite materials, a deep understanding of the electronic structure, interfacial charge distribution, adsorption energies, and structural stability can be provided by DFT. For instance, investigation of the charge transfer between MXene surfaces with conjugated organic molecules using DFT showed the improved conductivity and interfacial electron mobility in the hybrid structure [209]. Also, DFT has revealed the important role of linkers in tailoring the band gaps, porosity, and redox performance of COF-based materials [210]. Optimization of these factors using DFT can guide us in the fabrication of COF@MXene composites with better performance for applications such as energy storage, sensing, and electrocatalysis.

A key note in the computational modeling is its ability to optimize the interaction between COF linkers and MXene terminal groups (–OH, –F, –O) to provide the highest stability and best performance in the targeted applications. For instance, DFT studies showed that the electronic conductivity of fluorinated MXenes is lower than that of hydroxylated MXenes [211]. Therefore, computational screening can help in providing stronger synergistic effects between the hybrid architectures

Furthermore, combining machine learning (ML) with DFT can help in the development of new COF@MXene hybrids by finding the structure-performance relationships. These integrated approaches are especially valuable for identifying candidate materials for high-performance supercapacitors, batteries, and catalytic applications.

Molecular dynamics (MD) simulations and Monte Carlo methods can provide additional insights into ion transport, mechanical properties, and stability under practical conditions. Indeed, the device design and material selection can be refined by connecting the theoretical predictions with practical applications through computational modeling.

To use the full potential of COF@MXene hybrids, it is important to integrate the experimental data with the computational prediction tools to shorten the development of newer COF@MXene hybrids with stronger performances.

8. Future Perspectives: Challenges and Potential of COF@MXene Hybrids

The COF@MXene hybrids can be considered among frontiers in advanced materials due to the combination of unique features, including structural tunability, high surface area, electrical conductivity, and chemical performance. These hybrids are still in the early stages of their development. Although diverse types of MXenes have been synthesized, only $Ti_3C_2T_x$ and Nb_2CT_x MXenes have been used to fabricate COF@MXene hybrids. Therefore, future studies are expected to involve other types of MXenes for the fabrication of different types of COF@MXene materials.

Similarly, while various types of COFs have been prepared, imine-based COFs are the main group that have been utilized in COF@MXene fabrication. It is important to mention that the imine COFs have poor stability under harsh conditions, including strong acids, bases, redox agents, and high temperatures. Therefore, the involvement of boronate-ester COFs, azine-based COFs, and imide-based COFs in future research can probably lead to the COF@MXene hybrids with higher stabilities under harsh conditions.

While COF@MXene hybrids have shown prominent performance in diverse applications, there are still challenges that need to be addressed, including: (i) scalability, (ii) chemical stability, (iii) interfacial control, and (iv) mechanistic understanding. (i) Scalability: complicated manufacturing processes make mass production of these hybrids a real challenge for practical use. Therefore, it is important to develop simpler and more efficient synthesis strategies. (ii) Chemical stability: Low chemical stability of MXenes in water and water-based colloidal solutions upon storage and poor structural robustness of COFs imposed by harsh environments require designing effective strategies for stabilization of these hybrid composites. (iii) Interfacial control: Enhancement of interfacial attachment between MXenes and COFs can further upgrade stability, lifetime, and performance of their composites.(iv) Mechanistic understanding: The governing mechanisms of the synergistic effects between MXenes and COFs should not be overlooked. A combination of experimental and theoretical studies could gain a deeper understanding of electron and ion transport mechanisms in these hybrid materials.

While addressing the above challenges can help to prepare COF@MXenes with stronger performances, at the same time, more advanced composites can be obtained by incorporating various nanomaterials or doping agents into the COF@MXene structure. MOFs, as the metal-containing analogs of COFs, have also been widely used for the fabrication of MOF@MXene hybrids [212]. Therefore, a bridge between COF@MXenes and MOF@MXenes can probably provide stronger synergistic effects. Indeed, in recent years, research on the development of metal-covalent organic frameworks (MCOFs) that combine the active metal centers of MOFs with the structural advantages of COFs has gained the attention of researchers [213–215]. It is expected that the hybridization of MCOFs with MXenes will address the limitations of individual COFs and MOFs and provide new hybrids with enhanced performance.

Regarding the application aspects, the COF@MXene hybrids have the potential to be further used in other sectors such as gas separation and purification, ion separation, adsorption, and diverse biomedical fields including, wound healing, drug delivery, and cancer therapy.

CRediT authorship contribution statement

Mostafa Dadashi Firouzjaei: Writing – review & editing, Writing – original draft. **Ahmad Arabi Shamsabadi:** Writing – review & editing, Writing – original draft. **Anupma Thakur:** Writing – review & editing, Writing – original draft. **Mark Elliott:** Writing – review & editing, Writing – original draft. **Babak Anasori:** Writing – review & editing, Writing – original draft, Supervision. **Farzad Seidi:** Writing – review & editing, Writing – original draft, Supervision. **Yuqian Liu:** Writing – review & editing, Writing – original draft. **Yang Huang:** Writing – review & editing, Writing – original draft. **Huining Xiao:** Writing – review & editing, Writing – original draft, Supervision.

Declaration of Competing Interest

The authors declare the following financial interests/personal relationships which may be considered as potential competing interests: Farzad Seidi reports financial support was provided by Foundation for Innovative Research Groups of the National Natural Science Foundation of China. If there are other authors, they declare that they have no known competing financial interests or personal relationships that could have appeared to influence the work reported in this paper.

Acknowledgment

This study was supported by the Provincial Key Lab of Pulp and Paper Science and Technology and Joint International Research Lab of Lignocellulosic Functional Materials, Nanjing Forestry University; the National Nature Science Foundation of China (Grant No.: 31730106, 31770623) and NSERC Canada. We also acknowledge funding support from the US National Science Foundation, award number CMMI-2134607.

Appendix A. Supporting information

Supplementary data associated with this article can be found in the online version at doi:10.1016/j.mser.2025.101087.

Data availability

No data was used for the research described in the article.

References

[1] Y. Wu, K. Zhang, B. Yang, Adv. Opt. Mater. 7 (2019) 1800980.
[2] A. Elmasry, W. Azoti, S.A. El-Safty, A. Elmarakbi, Prog. Mater. Sci. 132 (2023).
[3] H.-N. Barad, H. Kwon, M. Alarcón-Correa, P. Fischer, ACS Nano 15 (2021) 5861–5875.
[4] H. Jalali, R. Eslami-Farsani, B. Ramezanzadeh, Acc. Chem. Res. (2023).
[5] Z. Ye, Y. Bao, Z. Chen, H. Ye, Z. Feng, Y. Li, Y. Zeng, Z. Pan, D. Ouyang, K. Zhang, X. Liu, Y. He, Coord. Chem. Rev. 504 (2024) 215654.
[6] X. Gao, H. Wu, C. Su, C. Lu, Y. Dai, S. Zhao, X. Hu, F. Zhao, W. Zhang, I.P. Parkin, C.J. Carmalt, G. He, Energy Environ. Sci. 16 (2023) 1364–1383.
[7] C.M. Hui, J. Pietrasik, M. Schmitt, C. Mahoney, J. Choi, M.R. Bockstaller, K. Matyjaszewski, Chem. Mater. 26 (2014) 745–762.
[8] F. Seidi, M.R. Saeb, Y. Jin, P. Zinck, H. Xiao, MiniRev. Org. Chem. 19 (2022) 416–431.
[9] B. Wang, L. Shen, Y. He, C. Chen, Z. Yang, L. Fei, J. Xu, B. Li, H. Lin, Small N./a (2023) 2310174.
[10] F. Ahmadijokani, A. Ghaffarkhah, H. Molavi, S. Dutta, Y. Lu, S. Wuttke, M. Kamkar, O.J. Rojas, M. Arjmand, Adv. Funct. Mater. N./a (2023) 2305527.
[11] K. Jayaramulu, S. Mukherjee, D.M. Morales, D.P. Dubal, A.K. Nanjundan, A. Schneemann, J. Masa, S. Kment, W. Schuhmann, M. Otyepka, R. Zboril, R. A. Fischer, Chem. Rev. 122 (2022) 17241–17338.
[12] H. Saini, N. Srinivasan, V. Sedajova, M. Majumder, D.P. Dubal, M. Otyepka, R. Zboril, N. Kurra, R.A. Fischer, K. Jayaramulu, Acs Nano 15 (2021) 18742–18776.
[13] R.K. Sharma, S. Sharma, S. Dutta, R. Zboril, M.B. Gawande, Green. Chem. 17 (2015) 3207–3230.
[14] S.F. Hammad, I.A. Abdallah, A. Bedair, R.M. Abdelhameed, M. Locatelli, F. R. Mansour, TrAC Trends Anal. Chem. 170 (2024) 117425.
[15] X. Qi, Y. Xiang, E. Cai, X. Ge, X. Chen, W. Zhang, Z. Li, J. Shen, Coord. Chem. Rev. 496 (2023) 215426.
[16] J. Li, W. Lu, Y. Yang, R. Xiang, Y. Ling, C. Yu, Y. Zhou, Adv. Sci. 10 (2023).
[17] S. Ezendam, M. Herran, L. Nan, C. Gruber, Y. Kang, F. Groebmeyer, R. Lin, J. Gargiulo, A. Sousa-Castillo, E. Cortes, ACS Energy Lett. 7 (2022) 778–815.
[18] A. Gupta, S. Ghosh, M.K. Thakur, J. Zhou, K. Ostrikov, D. Jin, S. Chattopadhyay, Prog. Mater. Sci. 121 (2021).
[19] K. Mishra, N. Devi, S.S. Siwal, V.K. Gupta, V.K. Thakur, Adv. Sustain. Syst. 7 (2023).
[20] T. Ramachandran, F. Hamed, Y.A. Kumar, R.K. Raji, H. Hegazy, J. Energy Storage 73 (2023) 109299.
[21] M. Naguib, J. Come, B. Dyatkin, V. Presser, P.-L. Taberna, P. Simon, M. W. Barsoum, Y. Gogotsi, Electrochem. Commun. 16 (2012) 61–64.
[22] M. Naguib, O. Mashtalir, J. Carle, V. Presser, J. Lu, L. Hultman, Y. Gogotsi, M. W. Barsoum, ACS Nano 6 (2012) 1322–1331.
[23] M. Naguib, M. Kurtoglu, V. Presser, J. Lu, J. Niu, M. Heon, L. Hultman, Y. Gogotsi, M.W. Barsoum, Adv. Mater. 23 (2011) 4248–4253.
[24] P. Urbankowski, B. Anasori, T. Makaryan, D. Er, S. Kota, P.L. Walsh, M. Zhao, V. B. Shenoy, M.W. Barsoum, Y. Gogotsi, Nanoscale 8 (2016) 11385–11391.
[25] Q. Zhang, X. Meng, N. Yang, Gas Separation Technologies: MXenes-Based Membrane Systems, Age of MXenes, Volume 2. Applications in Diagnostics, Therapeutics, and Environmental Remediation, 1443, American Chemical Society, 2023, pp. 107–123.
[26] J. Zhu, E. Ha, G. Zhao, Y. Zhou, D. Huang, G. Yue, L. Hu, N. Sun, Y. Wang, L.Y. S. Lee, C. Xu, K.-Y. Wong, D. Astruc, P. Zhao, Coord. Chem. Rev. 352 (2017) 306–327.
[27] M. Downes, C.E. Shuck, B. McBride, J. Busa, Y. Gogotsi, Nat. Protoc. (2024).
[28] H. Ding, Y. Li, M. Li, K. Chen, K. Liang, G. Chen, J. Lu, J. Palisaitis, P.O. Persson, P. Eklund, Science 379 (2023) 1130–1135.
[29] T. Zhang, K. Shevchuk, R.J. Wang, H. Kim, J. Hourani, Y. Gogotsi, Chem. Mater. 36 (2024) 1998–2006.
[30] D. Wang, C. Zhou, A.S. Filatov, W. Cho, F. Lagunas, M. Wang, S. Vaikuntanathan, C. Liu, R.F. Klie, D.V. Talapin, Science 379 (2023) 1242–1247.
[31] J. Jeon, Y. Park, S. Choi, J. Lee, S.S. Lim, B.H. Lee, Y.J. Song, J.H. Cho, Y.H. Jang, S. Lee, ACS Nano 12 (2018) 338–346.
[32] X. Sang, Y. Xie, D.E. Yilmaz, R. Lotfi, M. Alhabeb, A. Ostadhossein, B. Anasori, W. Sun, X. Li, K. Xiao, P.R.C. Kent, A.C.T. van Duin, Y. Gogotsi, R.R. Unocic, Nat. Commun. 9 (2018) 2266.
[33] Z. Lin, L. Cai, W. Lu, Y. Chai, Small 13 (2017) 1700051.
[34] P. Urbankowski, B. Anasori, K. Hantanasirisakul, L. Yang, L. Zhang, B. Haines, S. J. May, S.J.L. Billinge, Y. Gogotsi, Nanoscale 9 (2017) 17722–17730.
[35] L. Verger, C. Xu, V. Natu, H.-M. Cheng, W. Ren, M.W. Barsoum, Curr. Opin. Solid State Mater. Sci. 23 (2019) 149–163.
[36] M. Alhabeb, K. Maleski, B. Anasori, P. Lelyukh, L. Clark, S. Sin, Y. Gogotsi, Chem. Mater. 29 (2017) 7633–7644.
[37] K.R.G. Lim, M. Shekhirev, B.C. Wyatt, B. Anasori, Y. Gogotsi, Z.W. Seh, Nat. Synth. 1 (2022) 14.
[38] M. Han, C.E. Shuck, R. Rakhmanov, D. Parchment, B. Anasori, C.M. Koo, G. Friedman, Y. Gogotsi, ACS Nano 14 (2020) 5008–5016.
[39] A. Thakur, B.S. N. Chandran, K. Davidson, A. Bedford, H. Fang, Y. Im, V. Kanduri, B.C. Wyatt, S.K. Nemani, V. Poliukhova, Small Methods 7 (2023) 2300030.
[40] M. Alhabeb, K. Maleski, B. Anasori, P. Lelyukh, L. Clark, S. Sin, Y. Gogotsi, Chem. Mater. 29 (2017) 7633–7644.
[41] A.A. Shamsabadi, H. Fang, D. Zhang, A. Thakur, C.Y. Chen, A. Zhang, H. Wang, B. Anasori, M. Soroush, Y. Gogotsi, Z. Fakhraai, Small Methods 7 (2023) 2300568.
[42] F. Seidi, A. Arabi Shamsabadi, M. Dadashi Firouzjaei, M. Elliott, M.R. Saeb, Y. Huang, C. Li, H. Xiao, B. Anasori, Small (2023) 2206716.
[43] T.S. Mathis, K. Maleski, A. Goad, A. Sarycheva, M. Anayee, A.C. Foucher, K. Hantanasirisakul, C.E. Shuck, E.A. Stach, Y. Gogotsi, ACS nano 15 (2021) 6420–6429.
[44] C. Xia, H. Ye, A. Kim, A. Sabahi Namini, S. Li, S.A. Delbari, J.Y. Park, D. Kim, Q. V. Le, R.S. Varma, R. Luque, A. T-Raissi, H.W. Jang, M. Shokouhimehr, Chemosphere 325 (2023) 138323.
[45] A.P. Isfahani, A.Arabi Shamsabadi, M. Soroush, Ind. Eng. Chem. Res. 62 (2023) 2309–2328.
[46] M. Mozafari, A. Arabi Shamsabadi, A. Rahimpour, M. Soroush, Adv. Mater. Technol. 6 (2021) 2001189.
[47] A. Sinha, Dhanjai, S.M. Mugo, J. Chen, K.S. Lokesh, 14 - MXene-based sensors and biosensors: next-generation detection platforms, in: C. Mustansar Hussain (Ed.), Handbook of Nanomaterials in Analytical Chemistry, Elsevier, 2020, pp. 361–372.
[48] X. Jiang, A.V. Kuklin, A. Baev, Y. Ge, H. Ågren, H. Zhang, P.N. Prasad, Phys. Rep. 848 (2020) 1–58.
[49] A.Arabi Shamsabadi, M. Sharifian Gh, B. Anasori, M. Soroush, ACS Sustain. Chem. Eng. 6 (2018) 16586–16596.
[50] K. Maleski, V.N. Mochalin, Y. Gogotsi, Chem. Mater. 29 (2017) 1632–1640.
[51] F. Cao, Y. Zhang, H. Wang, K. Khan, A.K. Tareen, W. Qian, H. Zhang, H. Ågren, Adv. Mater. 34 (2022) 2107554.
[52] H. Shin, H. Lee, Y. Seo, W. Jeong, T.H. Han, Langmuir 39 (2023) 2358–2367.
[53] S. Jung, U. Zafar, L.S.K. Achary, C.M. Koo, EcoMat 5 (2023) e12395.
[54] T. Su, X. Ma, J. Tong, H. Ji, Z. Qin, Z. Wu, J. Mater. Chem. A 10 (2022) 10265–10296.
[55] H. Riazi, M. Anayee, K. Hantanasirisakul, A.A. Shamsabadi, B. Anasori, Y. Gogotsi, M. Soroush, Adv. Mater. Interfaces 7 (2020) 1902008.
[56] X. Liu, A. Dang, T. Li, T.-C. Lee, Y. Sun, Y. Liu, F. Ye, S. Ma, Y. Yang, W. Deng, Biosens. Bioelectron. 237 (2023) 115531.
[57] S. Lim, H. Park, J. Yang, C. Kwak, J. Lee, Colloids Surf. A Physicochem. Eng. Asp. 579 (2019) 123648.
[58] A.P. Isfahani, A.A. Shamsabadi, F. Alimohammadi, M. Soroush, J. Hazard. Mater. 434 (2022) 128780.
[59] D. Li, Y. Luo, D. Onidas, L. He, M. Jin, F. Gazeau, J. Pinson, C. Mangeney, Adv. Colloid Interface Sci. 294 (2021) 102479.
[60] Y. Liu, Z. Dai, W. Zhang, Y. Jiang, J. Peng, D. Wu, B. Chen, W. Wei, X. Chen, Z. Liu, Z. Wang, F. Han, D. Ding, L. Wang, L. Li, Y. Yang, Y. Huang, ACS Nano 15 (2021) 9065–9075.
[61] Y. Lei, Y. Cui, Q. Huang, J. Dou, D. Gan, F. Deng, M. Liu, X. Li, X. Zhang, Y. Wei, Ceram. Int. 45 (2019) 17653–17661.
[62] P. Zhang, L. Wang, K. Du, S. Wang, Z. Huang, L. Yuan, Z. Li, H. Wang, L. Zheng, Z. Chai, W. Shi, J. Hazard. Mater. 396 (2020) 122731.
[63] J.E. Heckler, G.R. Neher, F. Mehmood, D.B. Lioi, R. Pachter, R. Vaia, W. J. Kennedy, D. Nepal, Langmuir 37 (2021) 5447–5456.
[64] G.S. Lee, T. Yun, H. Kim, I.H. Kim, J. Choi, S.H. Lee, H.J. Lee, H.S. Hwang, J. G. Kim, D.-W. Kim, H.M. Lee, C.M. Koo, S.O. Kim, Acs Nano 14 (2020) 11722–11732.
[65] C. Queffelec, M. Petit, P. Janvier, D.A. Knight, B. Bujoli, Chem. Rev. 112 (2012) 3777–3807.
[66] D. Kim, T.Y. Ko, H. Kim, G.H. Lee, S. Cho, C.M. Koo, ACS Nano 13 (2019) 13818–13828.
[67] Q. Feng, F. Deng, K. Li, M. Dou, S. Zou, F. Huang, Colloids Surf. A Physicochem. Eng. Asp. 625 (2021) 126903.

[68] M.-A. Neouze, U. Schubert, Chemical monthly, Mon. F. üR. Chem. 139 (2008) 183–195.
[69] J.T. Lee, B.C. Wyatt, G.A. Davis Jr., A.N. Masterson, A.L. Pagan, A. Shah, B. Anasori, R. Sardar, ACS Nano 15 (2021) 19600–19612.
[70] V. Natu, M. Sokol, L. Verger, M.W. Barsoum, J. Phys. Chem. C. 122 (2018) 27745–27753.
[71] R. Bian, R. Lin, G. Wang, G. Lu, W. Zhi, S. Xiang, T. Wang, P.S. Clegg, D. Cai, W. Huang, Nanoscale 10 (2018) 3621–3625.
[72] M. Carey, Z. Hinton, V. Natu, R. Pai, M. Sokol, N.J. Alvarez, V. Kalra, M. W. Barsoum, Cell Rep. Phys. Sci. 1 (2020) 100042.
[73] T.Y. Ko, D. Kim, S.J. Kim, H. Kim, A.S. Nissimagoudar, S.-C. Lee, X. Lin, P. T. Cummings, S. Doo, S. Park, T. Hassan, T. Oh, A. Chae, J. Lee, Y. Gogotsi, I. In, C.M. Koo, ACS Nano (2022).
[74] G. Ghanashyam, C.-S. Han, Desalination 601 (2025) 118597.
[75] A.P. Côté, A.I. Benin, N.W. Ockwig, M. O'Keeffe, A.J. Matzger, O.M. Yaghi, Science 310 (2005) 1166–1170.
[76] B. Zhang, M. Wei, H. Mao, X. Pei, S.A. Alshmimri, J.A. Reimer, O.M. Yaghi, J. Am. Chem. Soc. 140 (2018) 12715–12719.
[77] S. Bi, C. Yang, W. Zhang, J. Xu, L. Liu, D. Wu, X. Wang, Y. Han, Q. Liang, F. Zhang, Nat. Commun. 10 (2019) 2467.
[78] X. Guan, H. Li, Y. Ma, M. Xue, Q. Fang, Y. Yan, V. Valtchev, S. Qiu, Nat. Chem. 11 (2019) 587–594.
[79] J. Hu, Z. Huang, Y. Liu, Angew. Chem. Int. Ed. 62 (2023) e202306999.
[80] B. Diaz de Grenu, J. Torres, J. Garcia-Gonzalez, S. Munoz-Pina, R. de los Reyes, A. M. Costero, P. Amoros, J.V. Ros-Lis, Chemsuschem 14 (2021) 208–233.
[81] J. Maschita, T. Banerjee, G. Savasci, F. Haase, C. Ochsenfeld, B.V. Lotsch, Angew. Chem. Int. Ed. 59 (2020) 15750–15758.
[82] B.P. Biswal, S. Chandra, S. Kandambeth, B. Lukose, T. Heine, R. Banerjeet, J. Am. Chem. Soc. 135 (2013) 5328–5331.
[83] M. Matsumoto, L. Valentino, G.M. Stiehl, H.B. Balch, A.R. Corcos, F. Wang, D. C. Ralph, B.J. Marinas, W.R. Dichtel, Chem 4 (2018) 308–317.
[84] K. Chen, A. Cai, T.-T. Li, ChemSusChem 16 (2023) e202300021.
[85] T. Skorjanc, D. Shetty, M. Valant, Acs Sens. 6 (2021) 1461–1481.
[86] S.C. Jesudass, S. Surendran, G. Janani, T.-H. Kim, U. Sim, Adv. Energy Mater. 13 (2023) 2301918.
[87] Y. Zhao, K. Feng, Y. Yu, Adv. Sci. N./a (2023) 2308087.
[88] J. Aslam, M.A. Waseem, Y. Wu, W. Sun, Y. Wang, Adv. Colloid Interface Sci. 341 (2025) 103479.
[89] X.-M. Lu, J. Aslam, M.A. Waseem, Y. Zhang, W. Sun, Y. Wang, Coord. Chem. Rev. 535 (2025) 216604.
[90] D.W. Burke, Z. Jiang, A.G. Livingston, W.R. Dichtel, Adv. Mater. N./a (2023) 2300525.
[91] A. Knebel, J. Caro, Nat. Nanotechnol. 17 (2022) 911–923.
[92] S. Huang, K. Chen, T.-T. Li, Coord. Chem. Rev. 464 (2022).
[93] T. He, Y. Zhao, Angew. Chem. Int. Ed. 62 (2023) e202303086.
[94] L. Liu, D. Cui, S. Zhang, W. Xie, C. Yao, N. Xu, Y. Xu, Dalton Trans. 52 (2023) 6138–6145.
[95] B.-J. Yao, X.-M. Zhang, F. Li, C. Li, Y.-B. Dong, ACS Appl. Nano Mater. 3 (2020) 10360–10368.
[96] Y.-N. Gong, J.-H. Mei, W.-J. Shi, J.-W. Liu, D.-C. Zhong, T.-B. Lu, Angew. Chem. Int. Ed. N./a (2023) e202318735.
[97] Q. Ai, Q. Fang, J. Liang, X. Xu, T. Zhai, G. Gao, H. Guo, G. Han, L. Ci, J. Lou, Nano Energy 72 (2020).
[98] K. Geng, T. He, R. Liu, S. Dalapati, K.T. Tan, Z. Li, S. Tao, Y. Gong, Q. Jiang, D. Jiang, Chem. Rev. 120 (2020) 8814–8933.
[99] H. Wang, C. Qian, J. Liu, Y. Zeng, D. Wang, W. Zhou, L. Gu, H. Wu, G. Liu, Y. Zhao, J. Am. Chem. Soc. 142 (2020) 4862–4871.
[100] D. Guo, F. Ming, D.B. Shinde, L. Cao, G. Huang, C. Li, Z. Li, Y. Yuan, M.N. Hedhili, H.N. Alshareef, Adv. Funct. Mater. 31 (2021) 2101194.
[101] I. Janica, V. Montes-García, F. Urban, P. Hashemi, A.S. Nia, X. Feng, P. Samorì, A. Ciesielski, Small Methods 7 (2023) 2201651.
[102] R. Meng, Q. Deng, C. Peng, B. Chen, K. Liao, L. Li, Z. Yang, D. Yang, L. Zheng, C. Zhang, J. Yang, Nano Today 35 (2020) 100991.
[103] B. Sun, C.-H. Zhu, Y. Liu, C. Wang, L.-J. Wan, D. Wang, Chem. Mater. 29 (2017) 4367–4374.
[104] J.W. Colson, A.R. Woll, A. Mukherjee, M.P. Levendorf, E.L. Spitler, V.B. Shields, M.G. Spencer, J. Park, W.R. Dichtel, Science 332 (2011) 228–231.
[105] C. Ma, H. He, J. Qin, L. Luo, Y. Lan, J. Zhang, L. Yang, Q. Jiang, H. Huang, Small Struct. 5 (2024) 2300279.
[106] D. Guo, F. Ming, D.B. Shinde, L. Cao, G. Huang, C. Li, Z. Li, Y. Yuan, M.N. Hedhili, H.N. Alshareef, Z. Lai, Adv. Funct. Mater. 31 (2021) 2101194.
[107] P. Li, H. Lv, Z. Li, X. Meng, Z. Lin, R. Wang, X. Li, Adv. Mater. 33 (2021) 2007803.
[108] H. He, S. Chen, W. Bi, X. Wen, S. Sun, P. Zhang, R. Shen, X. Li, Sol. RRL 7 (2023) 2300532.
[109] M. Xu, Z. Li, R. Shen, X. Zhang, Z. Zhang, P. Zhang, X. Li, Chin. J. Catal. 70 (2025) 431–443.
[110] J. Qu, T. Yang, P. Zhang, F. Yang, Y. Cai, X. Yang, C.M. Li, J. Hu, Appl. Catal. B Environ. Energy 348 (2024) 123827.
[111] P. Wei, J. Dong, X. Gao, L. Chang, Z. Huang, H. Zheng, S.M.-Y. Lee, W.-Y. Lou, C. Peng, ACS Sustain. Chem. Eng. 12 (2024) 6881–6893.
[112] H. Zheng, Z. Huang, P. Wei, Y. Lin, Y. Cao, X. Zhang, B. Zhou, C. Peng, ACS Sustain. Chem. Eng. 13 (2025) 4078–4092.
[113] W. Wang, C. Liu, M. Zhang, C. Zhang, L. Cao, C. Zhang, T. Liu, D. Kong, W. Li, S. Chen, J. Colloid Interface Sci. 608 (2022) 735–748.
[114] C. Liu, W. Wang, M. Zhang, C. Zhang, C. Ma, L. Cao, D. Kong, H. Feng, W. Li, S. Chen, Chem. Eng. J. 430 (2022) 132663.
[115] H. Zong, S. Gong, K. Yu, Z. Zhu, ACS Appl. Nano Mater. 5 (2022) 15042–15052.
[116] H. He, H.-M. Wen, H.-K. Li, P. Li, J. Wang, Y. Yang, C.-P. Li, Z. Zhang, M. Du, Adv. Sci. 10 (2023) 2206933.
[117] L. Yue, Q. Jiang, L. Ma, Y. Li, L. Yang, J. Zhang, H. He, H. Huang, Chem. Mater. 37 (2025) 2125–2135.
[118] T. Simon, N. Bouchonville, M.J. Berr, A. Vaneski, A. Adrović, D. Volbers, R. Wyrwich, M. Döblinger, A.S. Susha, A.L. Rogach, F. Jäckel, J.K. Stolarczyk, J. Feldmann, Nat. Mater. 13 (2014) 1013–1018.
[119] Y. Peng, M. Zhao, B. Chen, Z. Zhang, Y. Huang, F. Dai, Z. Lai, X. Cui, C. Tan, H. Zhang, Adv. Mater. 30 (2018) 1705454.
[120] F.-M. Zhang, J.-L. Sheng, Z.-D. Yang, X.-J. Sun, H.-L. Tang, M. Lu, H. Dong, F.-C. Shen, J. Liu, Y.-Q. Lan, Angew. Chem. Int. Ed. 57 (2018) 12106–12110.
[121] S. Lu, Y. Hu, S. Wan, R. McCaffrey, Y. Jin, H. Gu, W. Zhang, J. Am. Chem. Soc. 139 (2017) 17082–17088.
[122] X. Zheng, Y. Song, Y. Liu, Y. Yang, D. Wu, Y. Yang, S. Feng, J. Li, W. Liu, Y. Shen, X. Tian, Coord. Chem. Rev. 475 (2023) 214898.
[123] A. Maier, L.M. Mguni, A.C.R. Ngo, D. Tischler, ChemCatChem 16 (2024) e202401021.
[124] Y. Zheng, C. Qi, Y. Qiao, K. Liu, Y. Wang, W. Jiang, Y. Jiang, F. Xin, F. Guo, W. Zhang, M. Jiang, Biotechnol. Adv. 82 (2025) 108600.
[125] G. Zhao, C. Yang, W. Meng, X. Huang, J. Mater. Chem. A 12 (2024) 3209–3229.
[126] J. Shi, C. Tao, Z. Wang, Y. Dai, S. Zhang, J. Li, Y. Chen, X. Mao, Z. Jiang, Angew. Chem. Int. Ed. N./a (2025) e202424995.
[127] V. Kumar, V. Singh, K.-H. Kim, E.E. Kwon, S.A. Younis, Coord. Chem. Rev. 447 (2021).
[128] D. Mei, L. Liu, B. Yan, Coord. Chem. Rev. 475 (2023) 214917.
[129] Y.-G. Wang, W. Jiang, X. Liu, L. Zhang, R.-P. Liang, J.-D. Qiu, Chem. Eng. J. 477 (2023) 146975.
[130] Z. Huang, M. Rafiq, A.R. Woldu, Q.-X. Tong, D. Astruc, L. Hu, Coord. Chem. Rev. 478 (2023) 214981.
[131] J. Deng, J.A. Iñiguez, C. Liu, Joule 2 (2018) 846–856.
[132] Z. Shan, Y. Sun, M. Wu, Y. Zhou, J. Wang, S. Chen, R. Wang, G. Zhang, Appl. Catal. BEnviron. Energy 342 (2024).
[133] L.-l Yu, J.-z Qin, W.-j Zhao, Z.-g Zhang, J. Ke, B.-j Liu, Int. J. Photo 2020 (2020).
[134] X. Fan, W. Chen, L. Xie, X. Liu, Y. Ding, L. Zhang, M. Tang, Y. Liao, Q. Yang, X.-Z. Fu, S. Luo, J.-L. Luo, Adv. Mater. 36 (2024) 2313179.
[135] M. Ahmad, M.B. Hussain, J. Chen, Y. Yang, X. Wu, H. Chen, S. Afzal, W. Raza, Z. Zeng, F. Ye, X. Zhao, J. Zhang, R. Feng, X.-Z. Fu, J.-L. Luo, ACS Catal. 14 (2024) 9134–9143.
[136] D. Liu, C. Zhang, G. Zhou, W. Lv, G. Ling, L. Zhi, Q.-H. Yang, Adv. Sci. 5 (2018).
[137] J. Wang, S. Yi, J. Liu, S. Sun, Y. Liu, D. Yang, K. Xi, G. Gao, A. Abdelkader, W. Yan, S. Ding, R.V. Kumar, ACS Nano 14 (2020) 9819–9831.
[138] Y. Zhang, Y. Wu, Y. Liu, J. Feng, Chem. Eng. J. 428 (2022) 131040.
[139] D. Zhang, S. Wang, B. Li, Y. Gong, S. Yang, Adv. Mater. 31 (2019) 1901820.
[140] G. Huang, J. Han, F. Zhang, Z. Wang, H. Kashani, K. Watanabe, M. Chen, Adv. Mater. 31 (2019).
[141] C. Niu, H. Pan, W. Xu, J. Xiao, J.-G. Zhang, L. Luo, C. Wang, D. Mei, J. Meng, X. Wang, Z. Liu, L. Mai, J. Liu, Nat. Nanotechnol. 14 (2019) 594–601.
[142] C. Wei, Y. Wang, Y. Zhang, L. Tan, Y. Qian, Y. Tao, S. Xiong, J. Feng, Nano Res. 14 (2021) 3576–3584.
[143] C. Wei, H. Fei, Y. An, Y. Tao, J. Feng, Y. Qian, J. Mater. Chem. A 7 (2019) 18861–18870.
[144] X. Li, Z. Zhang, D. Chen, F. Ma, J. Huang, Y. Wang, L. Wang, Y. Wu, Y. Chen, Adv. Funct. Mater. N./a (2025) 2505390.
[145] Z.A. Ghazi, X. He, A.M. Khattak, N.A. Khan, B. Liang, A. Iqbal, J. Wang, H. Sin, L. Li, Z. Tang, Adv. Mater. 29 (2017) 1606817.
[146] Y. Pang, J. Wei, Y. Wang, Y. Xia, Adv. Energy Mater. 8 (2018) 1702288.
[147] B. Wang, W. Guo, Y. Fu, ACS Appl. Mater. Interfaces 12 (2020) 5831–5837.
[148] L. Ye, S. Qi, T. Cheng, Y. Jiang, Z. Feng, M. Wang, Y. Liu, L. Dai, L. Wang, Z. He, ACS Nano 18 (2024) 18852–18869.
[149] L. Li, X. Chen, Z. Feng, Y. Jiang, L. Dai, J. Zhu, Y. Liu, L. Wang, Z. He, Green. Chem. 26 (2024) 6339–6360.
[150] T.T.K. Huynh, T. Yang, N. P S, Y. Yang, J. Ye, H. Wang, NanoMicro Lett. 17 (2025) 260.
[151] S. He, S. Chai, H. Li, ChemSusChem 18 (2025) e202402506.
[152] Y. Afzal, S. Ren, H. Wang, S. Ma, Q. Yuan, M.B. Zhao, X. Wadud, Q. Liang, G. Pan, Z. He, Jiang, J. Membr. Sci. 722 (2025) 123863.
[153] Y. Zhang, H. Liu, M. Liu, X. Li, Y. Zhang, H. Sun, H. Shi, Y. Feng, J. Membr. Sci. 714 (2025) 123410.
[154] X. Jia, Z. Lu, K. Huai, X. Yuan, Z. Yang, R. Huang, S. Zhai, Q. Ye, Z. Deng, J. Lin, S. He, J. Power Sources 637 (2025) 236592.
[155] W. Sun, F. Wang, B. Zhang, M. Zhang, V. Kuepers, X. Ji, C. Theile, P. Bieker, K. Xu, C. Wang, M. Winter, Science 371 (2021) 46.
[156] M. Li, Q. Yang, L. Fan, X. Dai, Z. Kang, R. Wang, D. Sun, ACS Appl. Mater. Interfaces 15 (2023) 39448–39460.
[157] Q. Cao, L. Wan, Z. Xu, W. Kuang, H. Liu, X. Zhang, W. Zhang, Y. Lu, Y. Yao, B. Wang, K. Liu, Adv. Mater. 35 (2023) 2210550.
[158] H. Zong, W. Liu, M. Li, S. Gong, K. Yu, Z. Zhu, ACS Appl. Mater. Interfaces 14 (2022) 10738–10746.
[159] M. Li, J. Liu, T. Zhang, X. Song, W. Chen, L. Chen, Small 17 (2021) 2005073.
[160] S. Kandambeth, V.S. Kale, O. Shekhah, H.N. Alshareef, M. Eddaoudi, Adv. Energy Mater. 12 (2022) 2100177.
[161] M. Hu, H. Zhang, T. Hu, B. Fan, X. Wang, Z. Li, Chem. Soc. Rev. 49 (2020) 6666–6693.
[162] Q. Geng, H. Wang, Y. Wu, L.-P. Lv, S. Chen, W. Sun, Y. Wang, ChemElectroChem 9 (2022) e202200340.

[163] N. An, Z. Guo, C. Guo, M. Wei, D. Sun, Y. He, W. Li, L. Zhou, Z. Hu, X. Dong, Chem. Eng. J. 458 (2023) 141434.

[164] M. Feng, Y. Zhang, X. Zhu, W. Chen, W. Lu, G. Wu, Angew. Chem. Int. Ed. 62 (2023) e202307195.

[165] X. Zhu, Y. Zhang, Z. Man, W. Lu, W. Chen, J. Xu, N. Bao, W. Chen, G. Wu, Adv. Mater. 35 (2023) 2307186.

[166] J. Wang, Z. Zhang, J. Zhu, M. Tian, S. Zheng, F. Wang, X. Wang, L. Wang, Nat. Commun. 11 (2020) 3540.

[167] L. Huang, L. Ding, J. Caro, H. Wang, Angew. Chem. Int. Ed. 62 (2023) e202311138.

[168] L. Huang, L. Ding, H. Wang, Small Sci. 1 (2021) 2100013.

[169] O. Mashtalir, K.M. Cook, V.N. Mochalin, M. Crowe, M.W. Barsoum, Y. Gogotsi, J. Mater. Chem. A 2 (2014) 14334–14338.

[170] L. Ding, L. Li, Y. Liu, Y. Wu, Z. Lu, J. Deng, Y. Wei, J. Caro, H. Wang, Nat. Sustain. 3 (2020) 296–302.

[171] H. Zhou, Y. Wang, F. Wang, H. Deng, Y. Song, C. Li, Z. Ling, Chin. Chem. Lett. 31 (2020) 1665–1669.

[172] Y. Sun, J. Lu, S. Li, C. Dai, D. Zou, W. Jing, Sep. Purif. Technol. 331 (2024) 125640.

[173] X. Liu, N. Graham, W. Yu, Y. Shi, K. Sun, T. Liu, J. Membr. Sci. 654 (2022) 120469.

[174] B.C. Wyatt, M.G. Boebinger, Z.D. Hood, S. Adhikari, P.P. Michałowski, S. K. Nemani, M.G. Muraleedharan, A. Bedford, W.J. Highland, P.R.C. Kent, R. R. Unocic, B. Anasori, Nat. Commun. 15 (2024) 6353.

[175] Y. Du, J. Yu, B. Chen, X. Zhu, Environmental Science Nano 12 (2025) 150–188.

[176] R. Ghanbari, D. Wu, P.M. Heynderickx, Coord. Chem. Rev. 523 (2025) 216253.

[177] L. Ding, Y. Wei, Y. Wang, H. Chen, J. Caro, H. Wang, Angew. Chem. Int. Ed. 56 (2017) 1825–1829.

[178] X. Gong, G. Zhang, H. Dong, H. Wang, J. Nie, G. Ma, J. Membr. Sci. 657 (2022) 120667.

[179] J. Wang, X. Xu, Y. Zhou, W. Ma, F. Wang, Y. Zhou, X. Men, Chem. Commun. 59 (2023) 8858–8861.

[180] Q. Li, X. Xu, J. Guo, J.P. Hill, H. Xu, L. Xiang, C. Li, Y. Yamauchi, Y. Mai, Angew. Chem. Int. Ed. 60 (2021) 26528–26534.

[181] C. Feng, K. Ou, Z. Zhang, Y. Liu, Y. Huang, Z. Wang, Y. Lv, Y.-E. Miao, Y. Wang, Q. Lan, T. Liu, J. Membr. Sci. 658 (2022) 120761.

[182] Z.-H. Wu, M. Wang, Y.-X. Ren, S. Li, X.-Y. Liu, Y. Cao, X.-Q. Wu, G. Hai, Z. Jiang, D.-S. Li, J. Membr. Sci. 701 (2024) 122755.

[183] J. Gao, L.-B. Huang, X. Meng, L. Xia, F. Yi, Z. He, Z. Pei, C. Hong, G. Wang, Y. Wang, Z. Jiang, Sep. Purif. Technol. 370 (2025) 133212.

[184] Y. Yang, Q. Liu, Y. Zou, M. Tian, L. Wang, L. Li, M. Wang, Y. Tao, J. Wang, Z. Wen, F. Ke, D. Wang, D. Gao, J. Environ. Chem. Eng. 11 (2023) 110975.

[185] J. Guo, X. Xu, J.P. Hill, L. Wang, J. Dang, Y. Kang, Y. Li, W. Guan, Y. Yamauchi, Chem. Sci. 12 (2021) 10334–10340.

[186] S. Huo, Y. Zhao, M. Zong, B. Liang, X. Zhang, I.U. Khan, X. Song, K. Li, J. Mater. Chem. A 8 (2020) 2505–2517.

[187] X. Xu, J. Tang, Y.V. Kaneti, H. Tan, T. Chen, L. Pan, T. Yang, Y. Bando, Y. Yamauchi, Mater. Horiz. 7 (2020) 1404–1412.

[188] S. Zhang, X. Xu, X. Liu, Q. Yang, N. Shang, X. Zhao, X. Zang, C. Wang, Z. Wang, J. G. Shapter, Y. Yamauchi, Mater. Horiz. 9 (2022) 1708–1716.

[189] N.J. Ronkainen, H.B. Halsall, W.R. Heineman, Chem. Soc. Rev. 39 (2010) 1747–1763.

[190] H. Liu, S. Ma, G. Ning, R. Zhang, H. Liang, F. Liu, L. Xiao, L. Guo, Y. Zhang, C.-P. Li, H. Zhao, Talanta 258 (2023) 124433.

[191] C. Haass, D.J. Selkoe, Nat. Rev. Mol. Cell Biol. 8 (2007) 101–112.

[192] Y. Lv, Y. Zhou, H. Dong, M. Xu, J. Zhang, M. Yan, Talanta 266 (2024) 125134.

[193] J. Cheng, K. Hu, Q. Liu, Y. Liu, H. Yang, J. Kong, Anal. Bioanal. Chem. 413 (2021) 2543–2551.

[194] H. Liu, S. Ma, G. Ning, R. Zhang, H. Liang, F. Liu, L. Xiao, L. Guo, Y. Zhang, C.-P. Li, Talanta 258 (2023) 124433.

[195] Q. Fei, Q. Huang, D. Nie, K. Fan, X. Wang, M. Bian, Z. Zhao, Z. Han, Microchem. J. 213 (2025) 113887.

[196] M. Sajid, M.K. Nazal, M. Rutkowska, N. Szczepanska, J. Namiesnik, J. Plotka-Wasylka, Crit. Rev. Anal. Chem. 49 (2019) 271–288.

[197] J. Feng, J. Feng, X. Ji, C. Li, S. Han, H. Sun, M. Sun, TrAC Trends Anal. Chem. 137 (2021) 116208.

[198] Y. Zhao, K. Hu, C. Yang, X. Liu, L. Li, Z. Li, P. Wang, Z. Zhang, S. Zhang, Anal. Chim. Acta 1237 (2023) 340581.

[199] J. Wu, Z. Wang, S. Zhang, Q. Yang, Z. Li, X. Zang, X. Zhao, N. Shang, N. Khaorapapong, X. Xu, Y. Yamauchi, Small N./a (2023) 2305730.

[200] C. Yang, N. Yang, D. Zhao, Z. Zhang, J. Song, Z. Zhang, K. Hu, S. Zhang, J. Chromatogr. A 1750 (2025) 465919.

[201] A. Sadanandan, S.A. Thomas, M.E. Khan, M.S. Alomar, M.R. Pallavolu, J. Cherusseri, Prog. Org. Coat. 183 (2023) 107757.

[202] S. Sharma, A. Kumar, E.E. Ebenso, Mater. Lett. 335 (2023) 133789.

[203] H. Cao, Composites Part B Engineering 271 (2024) 111168.

[204] J. Ding, H. Zhao, H. Yu, Chem. Eng. J. 430 (2022) 132838.

[205] Y. Ning, D. Jian, S. Liu, F. Chen, Y. Song, S. Li, B. Liu, Carbon 202 (2023) 20–30.

[206] M. Cai, X. Fan, H. Yan, Y. Li, S. Song, W. Li, H. Li, Z. Lu, M. Zhu, Chem. Eng. J. 419 (2021) 130050.

[207] B. Yang, G. Zhang, J. Dong, S. Tang, L. Zhang, Z. Wu, D. Bin, Y. Song, H. Lu, Int. J. Hydrog. Energy 47 (2022) 34244–34256.

[208] P. Najmi, N. Keshmiri, M. Ramezanzadeh, B. Ramezanzadeh, M. Arjmand, Chem. Eng. J. 456 (2023) 141001.

[209] G.R. Berdiyorov, M.E. Madjet, K.A. Mahmoud, Membranes 11 (2021) 543.

[210] L. Xu, T. Wu, P.R. Kent, D.-e Jiang, Phys. Rev. Mater. 5 (2021) 054007.

[211] J. Zhou, M. Khazaei, A. Ranjbar, V. Wang, T.D. Kühne, K. Ohno, Y. Kawazoe, Y. Liang, J. Mater. Chem. C. 8 (2020) 5211–5221.

[212] A. Chaouiki, M. Chafiq, R. Salghi, N. Elboughdiri, J.-H. Kang, Y.G. Ko, M. Abboud, J. Energy Chem. 104 (2025) 687–715.

[213] A. Altaf, I. Khan, A. Khan, S. Sadiq, M. Humayun, S. Khan, S. Zaman, A. Khan, R. A. Abumousa, M. Bououdina, ACS Omega 9 (2024) 34220–34242.

[214] T.H. Dolla, B. Zhang, T. Matthews, M.P. Chabalala, S.O. Ajayi, L.L. Sikeyi, X. Liu, M.K. Mathe, Coord. Chem. Rev. 518 (2024) 216061.

[215] Y. Fu, W. Zhang, H. Ma, ChemPlusChem 89 (2024) e202400236.

Farzad Seidi earned his PhD in organic and polymer chemistry from Sharif University of Technology in Iran in 2011. He is presently a professor at Nanjing Forestry University in China. His primary research interests lie in polymer and colloid chemistry and the development of polymeric and colloidal functional materials for applications in both biomedical and industrial fields. To date, he has authored more than 230 peer-reviewed articles.

Ahmad Arabi Shamsabadi received his Ph.D. in Chemical Engineering from Drexel University, U.S.A. Following his doctoral studies, he joined the University of Pennsylvania as a Postdoctoral Fellow at the Vagelos Institute for Energy Science and Technology (VIEST). Currently, he is a Principal R&D Scientist in Polymer Chemistry at Pall Corporation, New York. His research focuses on polymer membranes, gas and ion separation, water treatment, polymer thin films and composites, and polymer chemistry.

Dr. Mostafa Dadashi Firouzjaei is a Research Assistant Professor at the University of Alabama. Mostafa's professional background includes time as a doctoral student and a postdoctoral research associate in the Civil Engineering department at the University of Alabama. He holds a master's degree in Materials Engineering and Environmental Engineering. Mostafa received a BSc in Materials Science and Engineering in 2011. His study's main areas are the selection, characterization, and development of novel materials for water/wastewater treatment and microbiological disinfection. Since 2015, Mostafa began researching and developing methods for synthesizing novel antifouling and anti-biofouling polymeric membranes for sustainable water recovery.

Mark Elliott, PhD, is Professor of environmental engineering at the University of Alabama. His research focuses primarily on water and wastewater challenges in low-resources settings, wastewater management in the rural southeastern US, and membrane-based treatment of water and wastewater.

Dr. Anupma Thakur is a postdoctoral research associate in the School of Materials Engineering at Purdue University, working under the advisement of Prof. Babak Anasori. She earned her Ph.D. in Materials Science and Engineering from AcSIR, CSIR-CSIO, Chandigarh, India, as a Department of Science and Technology (DST) INSPIRE fellow in 2021. Her research focuses on the design and tailoring of 2D MXenes and 0D/1D nanomaterials for a wide range of applications, including photo/electrocatalysis for clean hydrogen energy generation, carbon capture and utilization, chemical sensing and environmental pollutant monitoring and degradation. Dr. Thakur has authored over 60 peer-reviewed international publications, contributing to the advancement of materials for energy and environmental applications.

Yang Huang received his Ph.D. degree from Nanjing University of Science and Technology (China) in 2017, majoring in chemical engineering and technology, followed by carrying out a postdoc work in The Hebrew University of Jerusalem (Israel). Now, he is an associate professor in the College of Science at Nanjing Forestry University (China). His current research centers on modification, regulation, and application of bacterial cellulose. Moreover, his interest falls into the area of electrochemical energy conversion and storage.

Yuqian Liu received his Ph.D. degree from Southeast University (China) in 2019, majoring in biomedical engineering. He is currently a lecturer in the College of Light Industry and Food Engineering at Nanjing Forestry University (China). His current research focuses on the fabrications of lignocellulosic biomass-based fluorescent complexes, and their applications in sensing, imaging, and anti-microbial. In addition, the mechanism study deep in the photoluminescence tuning, photodynamic, and photothermal phenomena of the emissive complexes is one of his main research contents.

Huining Xiao obtained his PhD in Chemical Eng. at McMaster University in Canada in 1995. Prior to working at the University of New Brunswick (UNB) Canada as Professor in 2001, he was a Lecturer at the University of Manchester in the UK from 1996 to 2001. His research interests focus on smart polymers and nanoparticles for functional-modified cellulose and green materials for the applications associated with barrier-enhanced packaging materials, personal protection equipment, the controlled release of agrochemicals and water/soil remediation.

Dr. Babak Anasori is the Reilly Rising Star Associate Professor at Purdue University, with joint appointments at the Schools of Materials Engineering and Mechanical Engineering. He received his PhD from Drexel University in 2014 in the Materials Science and Engineering Department, the birthplace of MXenes. He has authored over 200 refereed publications on MXenes and their precursors, and he has been recognized as a Web of Science Highly Cited Researcher since 2019. Dr. Anasori's research lab focuses on developing novel 2D carbide and carbonitride MXenes for various applications, including energy generation, electromagnetic interference shielding, and ultra-high temperature ceramics.